Check for updates

DFT analysis of the physical properties of direct band gap semiconducting double perovskites A$_2$BIrCl$_6$ (A = Cs, Rb; B = Na, K) for solar cells and optoelectronic applications†

Md. Tarekuzzaman, [a] Nazmul Shahadath,[a] Mufrat Montasir,[a] O. Alsalmi,[b] M. H. Mia,[cd] Hmoud Al-Dmour,[e] Md. Rasheduzzaman[a] and Md. Zahid Hasan [*a]

Double perovskite-based optoelectronic devices are gaining attention due to their unique characteristics, including a simple and stable crystal structure. This study employs density functional theory (DFT) with the full-potential linearized augmented plane-wave (FP-LAPW) method to investigate the structural, electronic, optical, mechanical, and thermodynamic properties of A$_2$BIrCl$_6$ (A = Cs, Rb; B = Na, K) double perovskite halides. The primary aim is to assess their potential applicability in optoelectronic devices and renewable energy technologies. The cubic stability of the predicted compounds was confirmed through the Goldsmith tolerance factor, octahedral factor, and a new tolerance factor. Additionally, to confirm their thermodynamic stability, we assessed the formation energy, binding energy, and phonon dispersion curves. We used the TB-mBJ potential to accurately predict the optoelectronic properties. The calculations of the electronic band structure indicated that the examined double perovskites exhibit a direct band gap semiconducting nature, with the following band gap values: 1.927 eV for Cs$_2$NaIrCl$_6$ 1.991 eV for Cs$_2$KIrCl$_6$, 2.025 eV for Rb$_2$NaIrCl$_6$, and 2.102 eV for Rb$_2$KIrCl$_6$. The A$_2$BIrCl$_6$ (A = Cs, Rb; B = Na, K) compounds demonstrate impressive optical properties, including low reflectivity and high light absorption coefficients (10^4 cm^{-1}) in the visible spectrum. Their spectral response extends from the visible to the UV range, making them ideal candidates for applications in solar cells and optoelectronic devices. The mechanical stability of the titled compounds was confirmed through the Born–Huang stability conditions based on their stiffness constants. The brittle nature of all the examined perovskites is confirmed by Pugh's ratio, Cauchy pressure, and Poisson's ratio. Finally, the Helmholtz free energy (F), internal energy (E), entropy (S), and specific heat capacity (C_v) are calculated based on the phonon density of states.

1. Introduction

The global energy crisis is intensifying daily because of increasing demand. For many years, burning fossil fuels like coal, oil (petroleum), and natural gas has released carbon dioxide and other pollutants into the atmosphere, which has led to environmental issues including air pollution and climate change. As a result, governments have had to look for alternative energy sources to replace coal, gasoline, oil, and other fossil fuels, which has been highlighted by the quick growth of technical developments and the escalating environmental concerns. Renewable energy can be a good option to lessen these effects on the environment. Renewable energy can be produced by decomposing organic waste, allowing for the capture and use of emitted gases for power production *via* generators. Moreover, solar and thermal energy conversion materials offer a sustainable alternative to environmentally harmful materials, particularly carbon-based fuels.[1,2] The two primary sources of renewable energy are solar energy and waste heat, which can be applicable in photovoltaic and thermoelectric procedures. Renewable energy sources like photovoltaics, thermoelectrics, and devices are great for the economy and technology since they are credible, affordable, and constantly functional. The capacity to execute thermal and photoelectric

aMaterials Research and Simulation Lab, Department of Electrical and Electronic Engineering, International Islamic University Chittagong, Kumira, Chittagong, 4318, Bangladesh. E-mail: zahidhasan.02@gmail.com

bDepartment of Physics, College of Science, Umm Al-Qura University, Makkah 21955, Saudi Arabia

cDepartment of Textile Engineering, Northern University Bangladesh, Uttara, Dhaka, Bangladesh

dDepartment of Computer and Communication Engineering, International Islamic University Chittagong, Kumira, Chattogram-4318, Bangladesh

eDepartment of Physics, Faculty of Science, Mutah University, karak 61710, Jordan

† Electronic supplementary information (ESI) available. See DOI: https://doi.org/10.1039/d5ra01748c

functions is contingent upon the selection of materials. The industry places great priority on the development of new solar cell technologies and materials with high inbuilt stability, high efficiency, and lower production costs. For the aforementioned procedures, perovskite halide materials are very promising. In the area of materials research, perovskite halides represent a fundamental change, as they provide a versatile substrate for a diverse array of usages, with solar power at the vanguard.

Halide perovskite materials have demonstrated remarkable capabilities as semiconductors, showcasing outstanding performance in applications like solar cells and lasers.[3,4] Hybrid perovskites, both organic and inorganic, have emerged as a prominent category of optoelectronic materials, showcasing record solar efficiencies alongside encouraging demonstrations of LEDs and transistors.[5–8] Innovative classes of perovskites, including double or complex halide perovskites have received significant attention for their exceptional efficiency and eco-friendliness.[9–11] Double perovskites are typically represented by the formula $A_2BB'X_6$, in which the A and B sites suggest the presence of a variety of elements.[12] Halide double perovskite photovoltaic cells have been stabilized through partial or complete substitution of the A-site/B-site cation and X-site anion.[13] The characteristics of halide double perovskites make them valuable in several fields, including photo-catalysis, storage gadgets, X-ray sensors, indoor photovoltaics, LEDs, and plenty more.[14–17] Furthermore, a single perovskite is limited to accommodating only the 2^+ cationic configuration in B-sites, while a double perovskite is capable of handling an even wider range, ranging from 1 to 4^+.[18] Because of this, the double perovskite provides better functionality, tunability, stability, lower defect density, band gap engineering flexibility, and continual usage advantages.

As a consequence, extensive investigations are underway to assess the viability of these materials for power generating applications. Perovskite materials, $CH_3NH_3PbI_3$, are composed of a hybrid organic–inorganic mixture and includes lead. The performance of these compounds in optoelectronic devices and solar cells has shown significant improvements, leading to enhanced efficiency.[19,20] The meticulous analysis carried out has led to a remarkable enhancement in efficiency, showing a substantial rise from 3.8% in 2009 to 25.2% in 2020. On top of that, improvements in this area have also raised efficiency which is now 29.1%.[21] They exhibit a direct energy band gap, a noticeable absorption in the visible spectrum, and stable electron–hole masses.[22,23] A combination of toxicity, environmental pollution, and health hazards makes Pb-based compounds less reliable. The radioactive instability of lead and its negative impacts on the environment make the substitution with other elements imperative. Consequently, there is an increasing need for nontoxic lead-free PSCs, prompting the development of various lead-free perovskite materials. In the pursuit of alternatives to lead-based perovskites, Pb^{2+} is being substituted with a range of nontoxic components, such as bivalent Sn^{2+} and Ge^{2+}.[24]

Nonetheless, replacing lead with Ge or Sn, which belong to the same group, is viewed as more advantageous; yet, this change results in a 10% decrease in efficiency.[25,26] A further layer of difficulty has been added due to the fact that Sn and Ge both exhibit variable valence electrons (+4, +2), which impacts their long-term endurance.[27] Additionally, Pb^{2+} has also been substituted with heterovalent M^{3+}, like Bi^{3+}, which is non-toxic, isoelectronic with Pb^{2+}, and exhibits stability in semiconducting halides.[28] Because their inherent trap densities and defect density are smaller, bismuth-based PSCs have longer charge carrier diffusion durations.[19] However, adding a highly charged Bi^{3+} ion to the lead-based perovskite also resulted in worse optoelectronic properties.[21,22] In addition, lead can be substituted with a complex mixture of monovalent and trivalent cations, whose structural formula is $A_2B'B''Z_6$. Here, "A" denotes a large cation (Rb + or Cs+), B′ and B″ denote trivalent or monovalent cations, and "Z" denotes oxygen or halogens. Recently, the halide perovskite $Cs_2InAgCl_6$, which is silver based, has been successfully synthesized and characterized.[29] Nevertheless, a large number of these perovskite materials show a deficient optical profile or a wide bandgap, which suggests they are only useful for limited functions in the industry of solar energy.

Additionally, scientific investigation has shown that the perovskite compound referred to as $Cs_2AgInCl_6$ features a direct bandgap and demonstrates significant stability. Regardless, adding more halides appears to make the perovskite structure less stable. The observed instability in perovskite materials could be associated with the presence of trapped states and structural defects, as indicated by the analysis of charge carrier relaxation and photoluminescence (PL).[30,31] In addition, the perovskite materials $Rb_2AgInCl_6$ and $Cs_2AgInCl_6$ have been shown to have substantial direct band gaps, which is very important when looking for compounds with outstanding solar capabilities.[32] Reports have been highlighted that the wide band gap In-based perovskites $X_2CuInCl_6$ (where X= Rb, K, or Cs) and Rb_2InSbX_6 (where X = Cl, Br) have remarkable optical absorption and thermoelectric characteristics.[33,34] Recent reports indicate that the wide band gap Na-based and K-based perovskite $Rb_2Na/KInX_6$ (where X = Br and I) are promising candidates for thermoelectric and solar energy uses.[35] A similar stable molecule, $Cs_2NaTlBr_6$, based on sodium, has been the subject of a recent theoretical investigation. With a straight bandgap of 1.82 eV, it now has a great chance of being used in photovoltaic applications.[36] Similarly, another study reported that Rb_2NaTlZ_6 (Z = Cl, Br, and I) have a direct band gap values of 3.4, 2.6, and 2.1 eV and he light absorption coefficients exhibited absorption in the visible and ultraviolet regions of the spectrum. Within these specific energy regions, there was very little loss of optical energy which suggests that these materials will be a promising candidate for optoelectronic and photovoltaic devices.[37] Furthermore, Cs_2InAsF_6, Cs = $RbIrF_6$, and Cs_2NaRhF_6 exhibit a direct band gap and values of 2.76 eV, 3.78 eV and 3.6 eV, respectively and they exhibit absorption in the ultraviolet (UV) region, indicating that they might be used as solar energy devices, laser and UV-shield components.[38]

The growing demand for optoelectronic devices underscores the importance of exploring and discovering additional members of the double perovskite family, despite the considerable research that has recently been conducted on various Cs

and Rb based double perovskites. Here in our investigation, we also examined another group of double perovskites, A_2BIrCl_6 (A = Cs, Rb; B = Na, K). Therefore, this study has examined the structural stability, optoelectronic characteristics, and thermoelectric characteristics of the A_2BIrCl_6 (A = Cs, Rb; B = Na, K) double perovskites. We believe that our research will provide crucial direction for forecasting lead-free DP materials that might be used in next solar cells and thermoelectric devices. The thermo-mechanical properties of the materials under study were also covered in this article as a standard evaluation.

2. Methodology

In this study, we utilized first-principles computations to explore the structural, dynamical, electronic, optical, mechanical, and thermophysical properties of the double perovskite A_2BIrCl_6 (A = Cs, Rb; B = Na, K). Through the density functional theory (DFT) approach,[39,40] the analysis was conducted using the Wien2k software, which is based on the FP-LAPW (Full-Potential Linearized Augmented Plane Wave) method and employs electronic wave functions.[41] In this process, the Generalized Gradient Approximation (GGA) with the Perdew–Burke–Ernzerhof (PBE)[42] approach is first employed to compute the ground state variables. Structural optimization is subsequently performed using the FP-LAPW method, guided by the third-order Birch–Murnaghan equation of state.[43] The plane wave cutoff parameter, denoted as $R_{MT} \times k_{max}$ was selected to be 8.0. Here, R_{MT} refers to the radius of the smallest atomic muffin-tin sphere, while k_{max} is the maximum wave vector in the plane wave basis. Within the muffin tin sphere, a maximum partial wave component of $l_{max} = 10$ was defined. The radii of the atomic muffin-tin spheres were set individually as follows: $R_{MT}(Cs) = 2.50$ a.u., $R_{MT}(K) = 2.13$ a.u., $R_{MT}(Ir) = 2.18$ a.u., and $R_{MT}(X) = 1.88$ a.u. To precisely represent the potential and charge density, we utilized a Fourier series incorporating wave vectors up to $G_{max} = 14$ $(Ry^{1/2})$. To ensure computational precision, a dense k-point mesh consisting of 1000 ($10 \times 10 \times 10$) points was utilized within the first Brillouin zone (BZ). During SCF calculations, the criteria for energy convergence (ec) and charge convergence (cc) are defined as 10^{-5} Ry and $0.001e$, respectively. The TB-mBJ (Trans Blaha modified Becke–Johnson)[44] methodology was applied to assess optoelectronic characteristics, balancing precision and computational efficiency for inorganic compounds. We used the same k-mesh of 1000 points ($10 \times 10 \times 10$) for both the structure optimizations and the Trans Blaha-modified Becke–Johnson methodology. VESTA software was used to visualize the crystal structure.[45] Additionally, using the Cambridge Serial Total Energy Package (CASTEP) code,[46] the materials phonon dynamic stability was verified. To calculate phonons, a $1 \times 1 \times 1$ supercell model of the unit cell structure was used. To assess the lattice dynamics, including phonon dispersion and thermodynamic properties, we utilized the supercell method with finite displacement. A cut-off energy of 500 eV is set for the plane-wave basis set. The convergence criteria are defined as 5×10^{-6} eV per atom for total energy, 5×10^{-4} Å for maximum displacement, 0.01 eV Å^{-1} for maximum force, and 0.02 GPa for maximum stress. To ensure accurate sampling of the reciprocal space, the Brillouin zone is integrated using a $2 \times 2 \times 2$ k-point grid, following the Monkhorst–Pack scheme.

3. Result and discussion

3.1 Structural properties and stability

Structural property analysis is fundamental for assessing various material characteristics, including the bandgap of semiconductors.[47] In addition, the structural characteristics offer a clear understanding of the basic atomic configuration and the volume of the unit cell. The chemical formula A_2BIrCl_6 (where A represents Cs or Rb, and B represents Na or K) is composed of four distinct elements (A, B, Ir, and Cl) in a ratio of 2 : 1 : 1 : 6. Double perovskites possess unique structural features and stability due to the combination of a large A-site cation and two distinct B-site cations. The typical crystal configuration of inorganic double halide perovskites A_2BIrCl_6 (A = Cs, Rb; B = Na, K) is depicted in Fig. 1. The double halide perovskites A_2BIrCl_6 (A = Cs, Rb; B = Na, K) crystallize in a cubic double-perovskite structure with an $Fm\bar{3}m$ space group. The unit cell of A_2BIrCl_6 (where A = Cs, Rb; B = Na, K) contains a total of 10 atoms, including 2 atoms of A, 1 atom of B, 1 atom of Ir, and 6 atoms of Cl. In the unit cell, Cs/Rb atoms are positioned at 4a (0, 0, 0), Na/K are at 4b (0.5, 0, 0), Ir occupies 8c
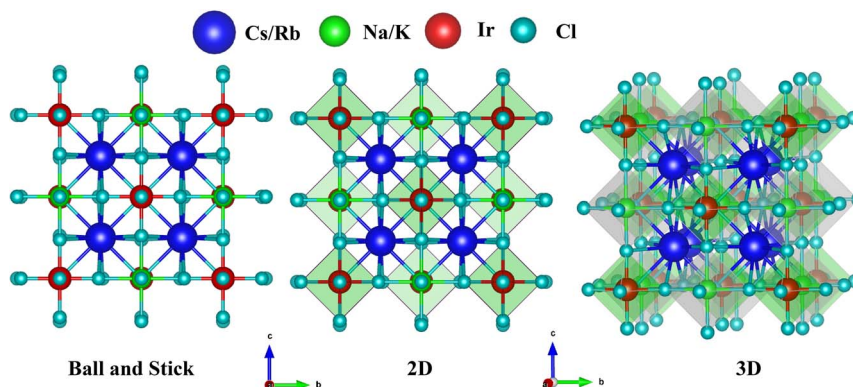

Fig. 1 Conventional crystal structures of A_2BIrCl_6 (A = Cs, Rb; B = Na, K).

Table 1 The lattice constant a_0 (Å), bulk modulus B_0 (GPa), first derivative of bulk modulus B_0', total energy E_{tot} (Ry), formation energy E_f (eV per atom), and binding energy E_B (eV per atom) for double perovskite (DP) A_2BIrCl_6 (A = Cs, Rb; B = Na, K)

DP	a_0 (Å)	B_0 (GPa)	B_0'	E_{tot} (Ry)	E_f (eV per atom)	E_b (eV per atom)	References
$Cs_2NaIrCl_6$	10.146	38.20	5.00	−72 741.20	−2.37	−4.39	This
Cs_2KIrCl_6	10.461	33.77	2.38	−73 620.50	−2.40	−4.37	This
$Rb_2NaIrCl_6$	10.022	39.83	4.93	−53 505.98	−2.33	−4.38	This
Rb_2KIrCl_6	10.359	33.12	2.80	−54 385.27	−2.34	−4.34	This

(0.25, 0.25, 0.75), and Cl is located at 24e (0.2513, 0, 0). The lattice parameters for $Cs_2NaIrCl_6$, Cs_2KIrCl_6, $Rb_2NaIrCl_6$, and Rb_2KIrCl_6 have been determined as 10.146 Å, 10.461 Å, 10.022 Å, and 10.359 Å, respectively. The estimated lattice parameter for the double perovskite (DP) A_2BIrCl_6 (A = Cs, Rb; B = Na, K) are tabulated in Table 1.

Additionally, the stability of double halide perovskites A_2BIrCl_6 (A = Cs, Rb; B = Na, K) can be evaluated through their formation energy and binding energy, derived from the given formulas.[48]

$$E_f = \frac{E_{A_2BIrCl_6} - n_A \times \dfrac{E_A}{k} - n_B \times \dfrac{E_B}{l} - n_{Ir} \times \dfrac{E_{Ir}}{m} - n_{Cl} \times \dfrac{E_{Cl}}{p}}{N} \tag{1}$$

$$E_b = E_{A2BIrCl6} - n_A \times \mu_A - n_B \times \mu_b - n_{Ir} \times \mu_{Ir} - n_{Cl} \times \mu_{Cl} \tag{2}$$

Here, $E_{A_2BIrCl_6}$ indicates the total energy of A_2BIrCl_6, and E_A, E_B, E_{Ir}, and E_C denote the energies of Cs/Rb, Na/K, Ir, and Cl atoms, respectively. The parameters n and μ indicate the number of Cs/Rb, Na/K, Ir, and Cl atoms, as well as the free-state energy of all the atoms combined. The constants k, l, m, and p represent the number of atoms in each unit cell, while N denotes the total number of atoms in the system. The negative formation energy confirms the stability, and a higher degree of negativity suggests stronger stability. As indicated in Table 1, all the materials examined show negative formation energy values, confirming their stability, with Cs_2KIrCl_6 being the most stable of the group. Fig. 2 demonstrates the energy variation with volume for all the compounds being studied.

To evaluate the stability of a double perovskite material, parameters such as the tolerance factor (τ_1), the physically derived new tolerance factor (τ_2), and the octahedral factor (μ) are used. Their values are determined from the formulas shown below:[49–51]

$$\tau_1 = \frac{R_A + R_{Cl}}{\sqrt{2}\left(\dfrac{R_B + R_{Ir}}{2} R_{Cl}\right)} \tag{3}$$

$$\tau_2 = \frac{R_{Cl}}{R_B} n_A \left(n_A - \frac{\dfrac{R_A}{R_B}}{\ln \dfrac{R_A}{R_B}}\right) \tag{4}$$
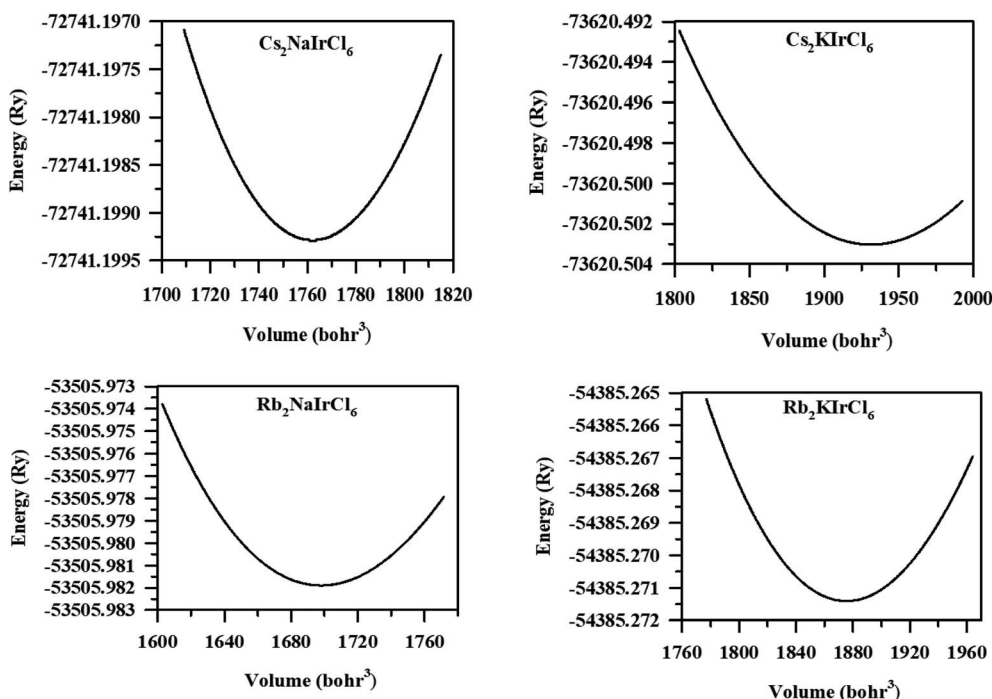
**Fig. 2** Birch–Murnaghan total energy *vs.* volume fitting curve for the A_2BIrCl_6 (A = Cs, Rb; B = Na, K).

Table 2 Shannon's ionic radii (r) of ions, Gold–Schmidt tolerance factor (t), octahedral factor (μ), and new tolerance factor (τ) for A_2BIrCl_6 (A = Cs, Rb; B = Na, K) compounds

DP	Ionic radius of cations (Å)		Ionic radius of anion (Å)	Tolerance factor (τ_1)	Octahedral factor (μ)	New tolerance factor (τ_2)
$Cs_2NaIrCl_6$	r_{Cs}	$\dfrac{(r_{Na} + r_{Ir})}{2}$	r_{Cl}	0.98	0.47	3.54
	1.88	0.85	1.81			
Cs_2KIrCl_6	r_{Cs}	$\dfrac{(r_{K} + r_{Ir})}{2}$	r_{Cl}	0.92	0.57	3.80
	1.88	1.03	1.81			
$Rb_2NaIrCl_6$	r_{Rb}	$\dfrac{(r_{Na} + r_{Ir})}{2}$	r_{Cl}	0.94	0.47	3.99
	1.72	0.85	1.81			
Rb_2KIrCl_6	r_{Rb}	$\dfrac{(r_{K} + r_{Ir})}{2}$	r_{Cl}	0.88	0.57	3.97
	1.72	1.03	1.81			

$$\mu = \frac{R_B + R_{Ir}}{2R_{Cl}} \qquad (5)$$

According to the eqn (3)–(5), R_A (Cs, Rb), R_B (Na, K), R_{Ir}, and R_{Cl} indicate the ionic radii of A (A = Cs, Rb), B (Na, K), Ir, and Cl, while n_A denotes the oxidation state of A (Cs, Rb). For a compound to exhibit cubic stability, its tolerance factor (τ_1), should range from 0.813 to 1.107,[49] while the octahedral factor (μ) must fall within 0.41 to 0.89.[51] The newly derived tolerance factor in our research demonstrates greater precision in forecasting structural stability than other approaches. Cubic stability in perovskites is expected when (τ_2), remains under 4.18.[50] We evaluated these parameters using Shannon's ionic radii. Table 2 illustrates that every compound analyzed maintains cubic structural stability.

Dynamic stability is crucial for ensuring durability and reliable performance of structures and materials under changing or fluctuating forces. Material stability is commonly analyzed through its phonon dispersion curve and phonon density of states (PHDOS). Phonons are crucial for understanding the dynamic behavior and thermal characteristics, which are key areas in materials science.[52] The dynamic stability of the A_2BIrCl_6 (A = Cs, Rb; B = Na, K) compound was evaluated by calculating the PDC and PHDOS at high symmetry K points (W-L-Γ-X-W-K) in the BZ, as shown in Fig. 3(a–d). The absence of imaginary frequencies across the Brillouin zone (BZ) signifies the dynamic stability of crystalline materials. In opposition, the presence of an imaginary component denotes dynamic instability. The absence of negative frequencies in the phonon dispersion curve (PDC) of A_2BIrCl_6 (A = Cs, Rb; B = Na, K) suggests its dynamic stability. In a compound with N atoms, the
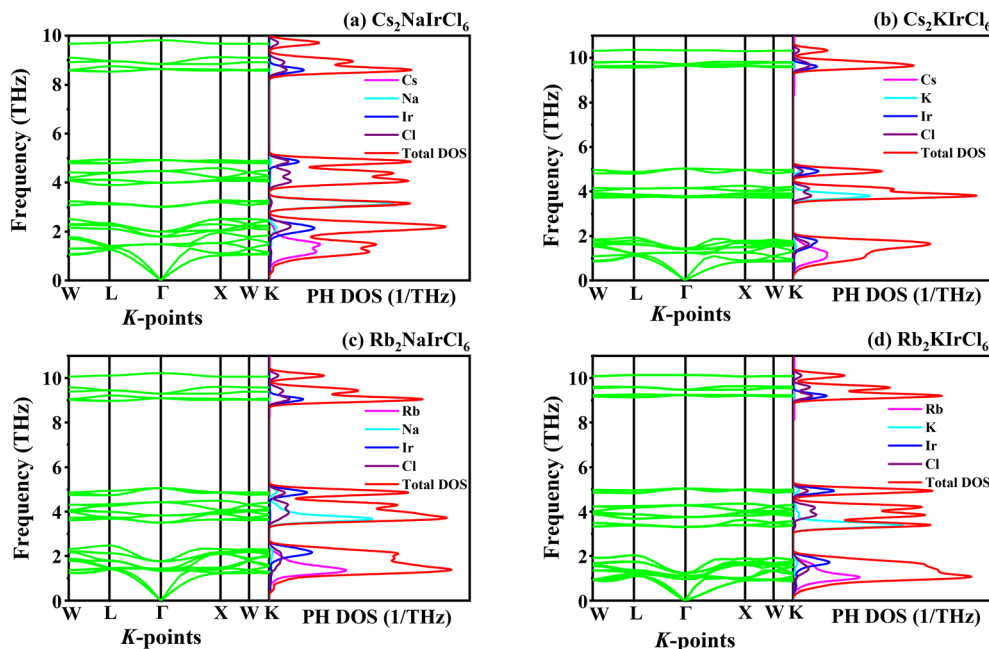
Fig. 3 Phonon dispersion curve along with phonon DOS of A_2BIrCl_6 (A = Cs, Rb; B = Na, K) compounds.

Table 3 Band gaps, band gap nature and calculated electron and hole effective mass values of DP A_2BIrCl_6 (A = Cs, Rb; B = Na, K) compounds

| Compounds	Band gap (eV)		Band gap nature	m_e^*		m_h^*	
	GGA + PBE	TB-mBJ		GGA + PBE	TB-mBJ	GGA + PBE	TB-mBJ
$Cs_2NaIrCl_6$	0.917	1.927	Direct	$0.21m_e$	$0.30m_e$	$1.33m_e$	$1.69m_e$
Cs_2KIrCl_6	1.048	1.991	Direct	$0.23m_e$	$0.32m_e$	$1.51m_e$	$1.98m_e$
$Rb_2NaIrCl_6$	0.971	2.025	Direct	$0.20m_e$	$0.29m_e$	$1.10m_e$	$1.41m_e$
Rb_2KIrCl_6	1.121	2.102	Direct	$0.23m_e$	$0.32m_e$	$1.24m_e$	$1.63m_e$

primitive cell contains 3N (3 × 10) vibrational modes. The A_2BIrCl_6 (A = Cs, Rb; B = Na, K) compound, with 10 atoms, exhibits 30 vibrational modes in total, including 27 optical modes and 3 acoustic modes. As illustrated in Fig. 3, the acoustic modes at the Γ-point are observed to be zero. For a better understanding of the compound's properties, its phonon DOS (PHDOS) is displayed next to the dispersion curve. The figure demonstrates that fluctuations in the PDC are depicted as smaller peaks, whereas flat dispersion in the PDC corresponds to prominent peaks in the PHDOS. The PHDOS

analysis reveals that the interaction between Cs/Rb and Cl atoms predominantly influences the lower-frequency phonon modes, while the Ir–Cl interaction produces the high-frequency phonon modes in all figures. Furthermore, the Na and K atoms significantly contribute to the middle-frequency phonon modes.

3.2 Electronic properties

To deepen our understanding of how the physical attributes of double perovskites (DPs) adapt with structural variations, it is
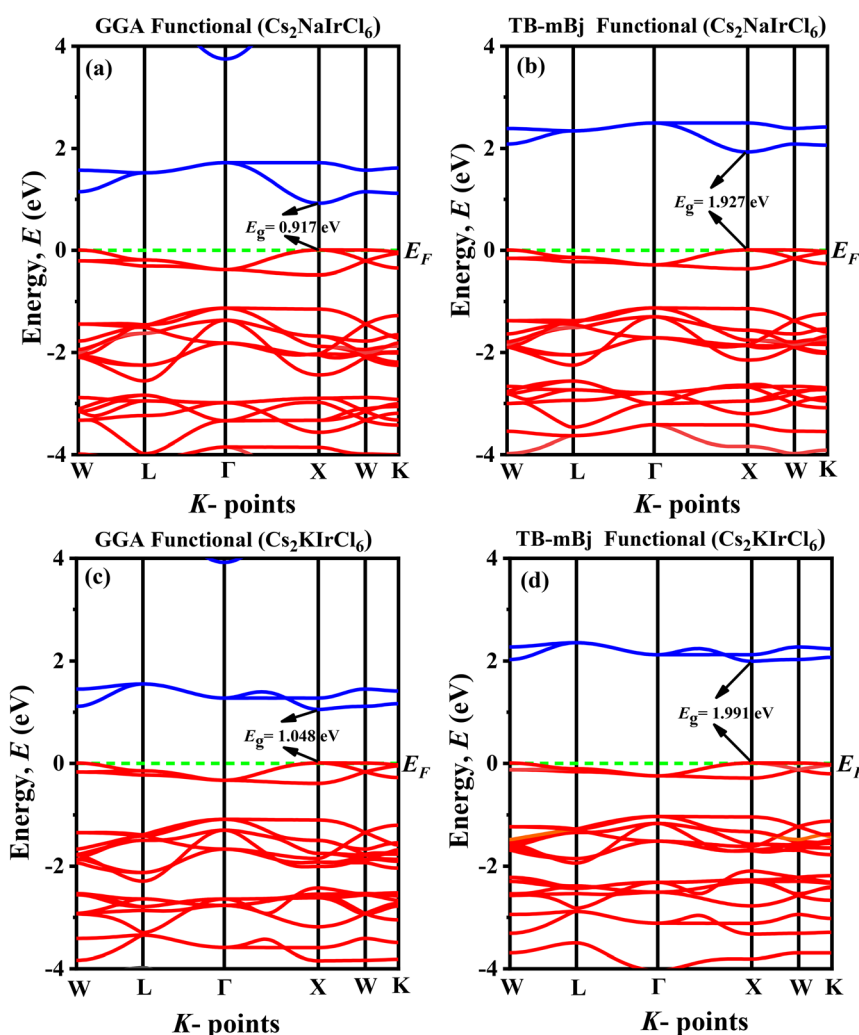
Fig. 4 Band diagram of (a) $Cs_2NaIrCl_6$ (GGA), (b) $Cs_2NaIrCl_6$ (TB-mBj), (c) Cs_2KIrCl_6 (GGA), (d) Cs_2KIrCl_6 (TB-mBj).
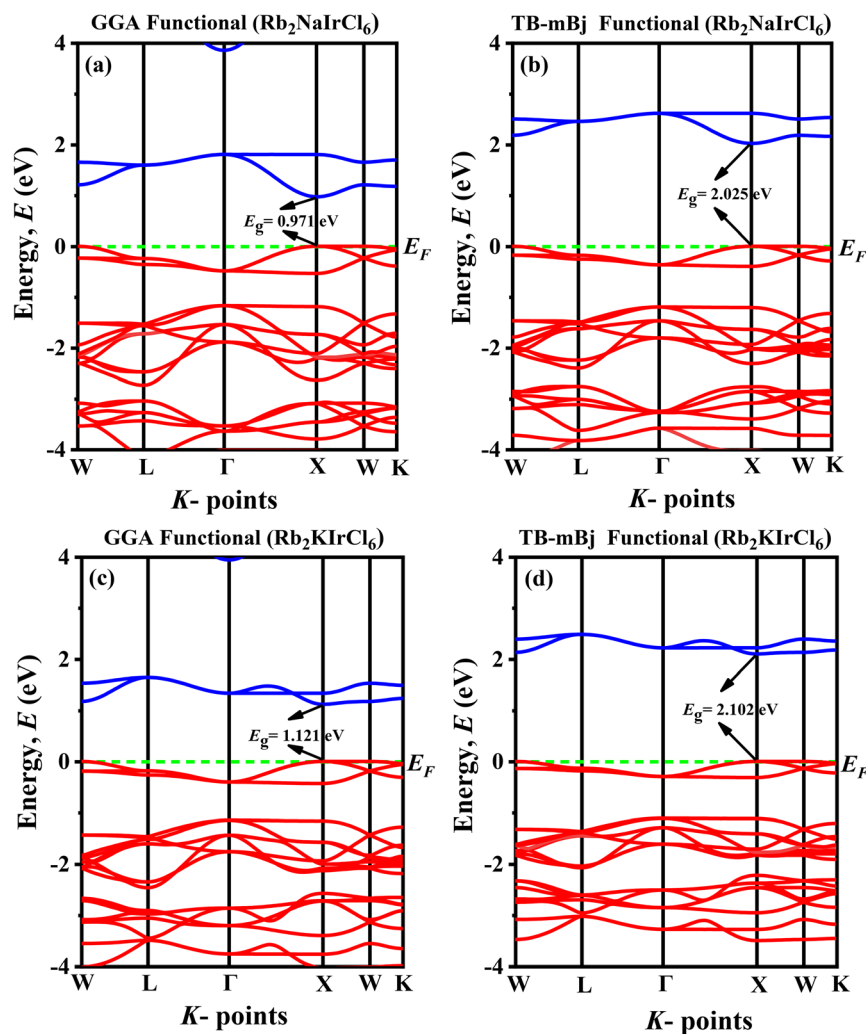
Fig. 5 Band diagram of (a) $Rb_2NaIrCl_6$ (GGA), (b) $Rb_2NaIrCl_6$ (TB-mBj), (c) Rb_2KIrCl_6 (GGA), (d) Rb_2KIrCl_6 (TB-mBj).

essential to analyze their electronic properties, particularly their band structures and partial density of states (PDOS). The calculated electronic band structures for A_2BIrCl_6 (A = Cs, Rb; B = Na, K) compounds, determined using GGA-PBE and the more advanced TB-mBJ functionals, are summarized in Table 3 and illustrated in Fig. 4 and 5. The Fermi level (E_F) is indicated by a horizontal green dashed line positioned at 0 eV for reference. Our computational findings reveal that the conduction band minimum (CBM) and valence band maximum (VBM) are both located at the X point in the Brillouin zone, irrespective of the functional used. This confirms that A_2BIrCl_6 (A = Cs, Rb; B = Na, K) compounds possess a direct bandgap, a highly desirable feature for semiconductors due to the superior efficiency of optical transitions it enables. Such a direct alignment is particularly advantageous for optoelectronic applications, including solar cells and light-emitting devices (LEDs), where high photon absorption and emission efficiencies are critical.

The bandgap values for the studied compounds range from 0.917 eV to 1.121 eV (GGA + PBE) and 1.927 eV to 2.102 eV (TB-mBJ), as seen in Table 3. The broader bandgap range calculated using TB-mBJ, renowned for its accuracy in bandgap

estimation, reflects a more reliable prediction of the electronic structure.[44] These bandgaps indicate the semiconducting nature of the materials and their suitability for visible-to-near-infrared (NIR) optoelectronic applications. Moreover, the substitution of smaller cations (e.g., Rb instead of Cs or K instead of Na) systematically increases the bandgap. This trend suggests a shift in optical absorption towards shorter wavelengths and enhanced insulating properties. These findings highlight the critical role of cation substitutions and lattice distortions in fine-tuning the electronic properties of these materials.

To further elucidate the band structures, the partial density of states (PDOS) and total density of states (TDOS) of the double perovskite compounds A_2BIrCl_6 (A = Cs, Rb; B = Na, K) were analyzed, as depicted in Fig. 6. The vertical dashed line at 0 eV represents the Fermi energy (E_F). A clear bandgap (E_g) is observed in the TDOS diagrams of all compounds, confirming their semiconducting nature. In the case of A_2BIrCl_6 (A = Cs, Rb; B = Na, K), the valence band is primarily derived from the Ir-5d and Cl-3p orbitals, while the conduction band is dominated by the Ir-5d orbitals with notable contributions from Cl-3p. The
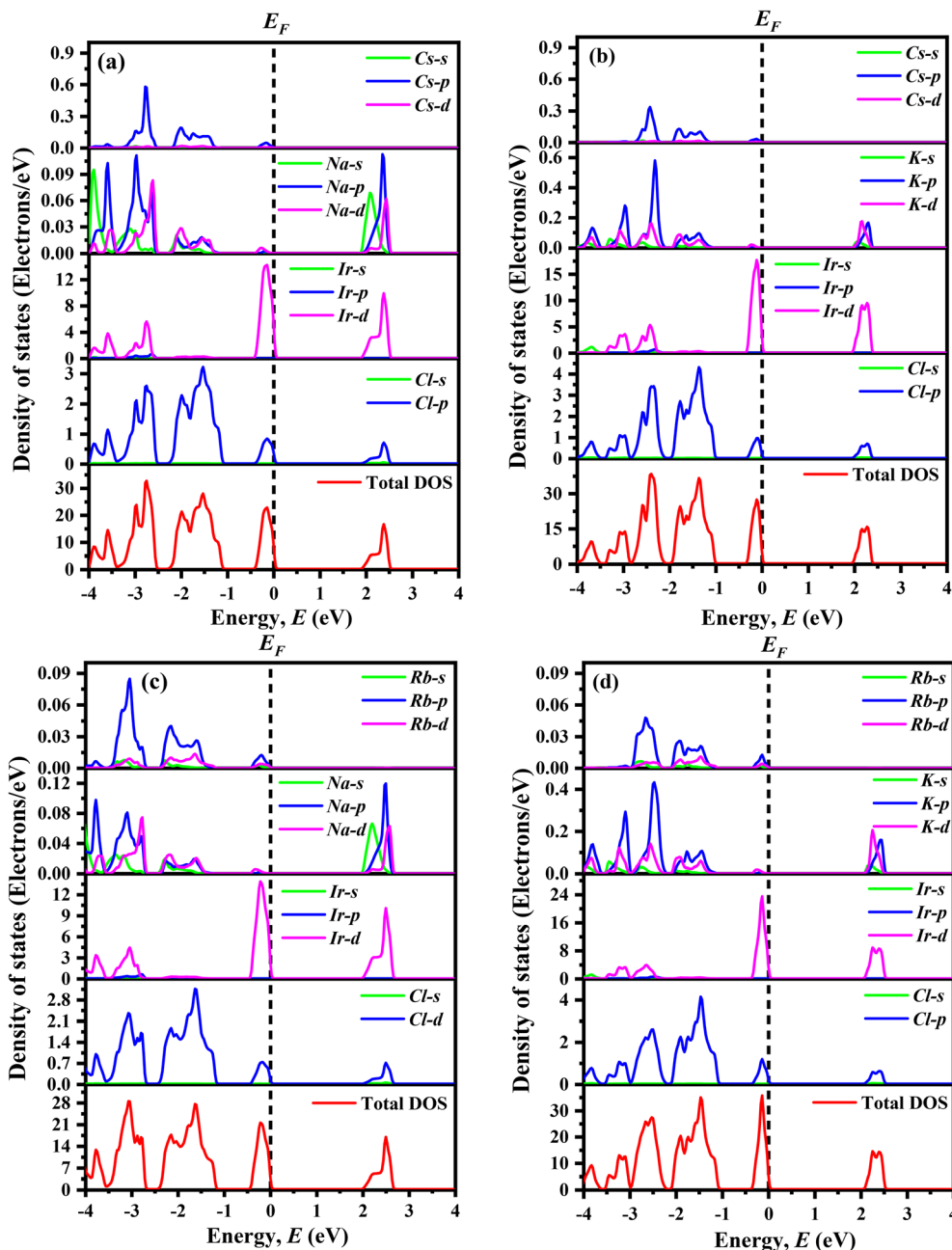
Fig. 6 Total DOS and partial DOS of (a) $Cs_2NaIrCl_6$, (b) Cs_2KIrCl_6, (c) $Rb_2NaIrCl_6$, (d) Rb_2KIrCl_6.

hybridization between Ir-5d and Cl-3p states plays a pivotal role in determining the electronic structure. Substitution of smaller cations (Rb instead of Cs or K instead of Na) enhances this hybridization, which increases the bandgap slightly and shifts the absorption toward shorter wavelengths. The negligible contributions of A-site and B-site cations to both the valence and conduction bands indicate that their role is primarily structural stabilization rather than active participation in electronic transitions. The Ir 5d orbitals are pivotal in defining the electronic structure, making Ir the principal determinant of the semiconducting and optoelectronic properties of these compounds.

The effective mass (m^*) is a key parameter that describes how electrons (m_e^*) and holes (m_h^*) respond to external forces, such as electric fields, within a semiconductor. A smaller effective mass for electrons or holes indicates higher mobility, leading to enhanced charge transport, which is crucial for optoelectronic device performance. The effective mass (m^*) of A_2BIrCl_6 (A = Cs, Rb; B = Na, K) is calculated by fitting the actual E–k curve around the conduction band minimum (CBM) and the valence band maximum (VBM) at the X-point. This calculation uses the equation:[53]

$$m^* = \hbar^2 \left(\frac{d^2 E}{dk^2} \right)^{-1} \tag{6}$$

where $\hbar$ is the reduced Planck's constant, E is the energy of the particle, and k is the wave vector. The effective masses of electrons (m_e^*) and holes (m_h^*) in A_2BIrCl_6 (A = Cs, Rb; B = Na, K) vary among the four compounds, reflecting differences in their electronic structures. Electron effective masses (m_e^*) are relatively low, ranging from 0.20–$0.23m_0$ (GGA + PBE) to 0.29–$0.32m_0$ (TB-mBJ), whereas hole effective masses (m_h^*) are higher, spanning 1.10–$1.51m_0$ (GGA + PBE) to 1.41–$1.98m_0$ (TB-mBJ). Among these, $Rb_2NaIrCl_6$ exhibits the lowest m_e^* and m_h^*, making it the most promising material for enhanced charge carrier mobility. Lower effective masses, as seen in $Rb_2NaIrCl_6$, enable higher carrier mobility, crucial for efficient charge transport in optoelectronic applications. In contrast, Cs_2KIrCl_6 has the highest m_h^*, indicating reduced hole mobility, which may hinder its performance in applications requiring balanced charge transport, such as solar cells and light-emitting devices. The variations in effective mass stem from structural and orbital factors. Smaller cations like Rb (*vs.* Cs) and Na (*vs.* K) introduce lattice distortions, enhancing orbital overlap and reducing effective mass. Additionally, strong Ir 5d–Cl 3p hybridization broadens the bands, lowering effective mass. Compounds with higher effective masses experience weaker hybridization and narrower bands.

3.3 Nature of bonding

Charge density mapping offers a method to study electron density in materials, giving clues about their bonding and electronic structures. This method identifies areas of high and low electron density in the crystal structure, providing insights into the nature of bonding, whether ionic, covalent, or metallic. Charge density mapping for A_2BIrCl_6 (A = Cs, Rb; B = Na, K) provides key insights into the bonding interactions among the constituent atoms. As a part of the double perovskite family, A_2BIrCl_6 (A = Cs, Rb; B = Na, K) exhibits captivating

Scale:	$\Delta n(r)$
■ (red)	+0.0007
■ (yellow)	+0.9174
■ (green)	+1.8341
■ (cyan)	+2.7509
■ (blue)	+3.6676
■ (magenta)	+4.5843
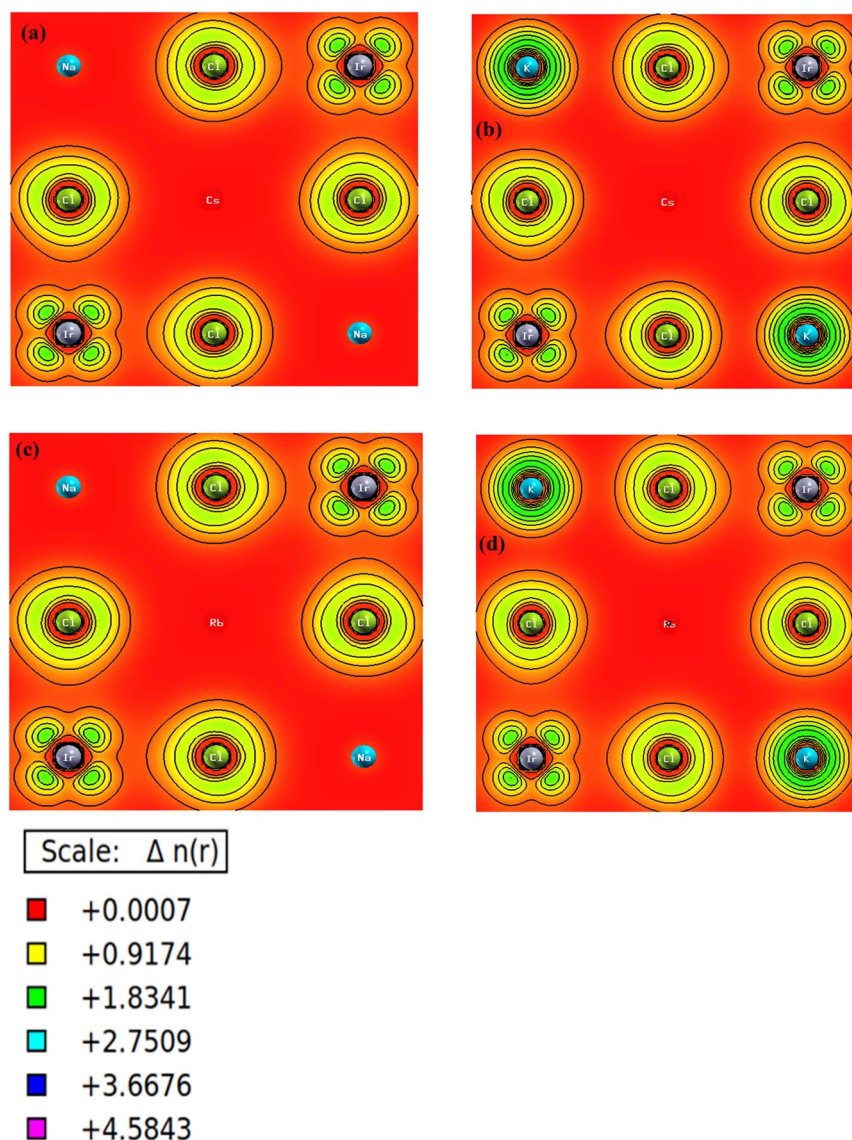
Fig. 7 Contour plot of charge density of (a) $Cs_2NaIrCl_6$, (b) Cs_2KIrCl_6, (c) $Rb_2NaIrCl_6$, and (d) Rb_2KIrCl_6.

characteristics due to its exceptional bonding and crystal framework. The cubic crystal structure of these materials, classified under space group $Fm\bar{3}m$, reflects the significant contributions of cations (Cs^+/Rb^+) and the lattice to their properties. In this configuration, the Cl ions are centrally located in the octahedra, while Na and K ions occupy the corners, sharing the octahedral spaces. The spaces between the Cs^+/Rb^+ ions create interstitial regions. This arrangement forms a network of octahedra connected at the corners, influencing the compound's electronic and bonding properties. Fig. 7 presents the charge density contour map for these compounds. The A ions (Cs/Rb) are more electronegative than B ions (Na, K), leading to ionic bonding with the nearby Cl ions. This leads to the formation of A–Cl bonds with a strong ionic character. The B (Na, K)–Ir–Cl octahedral structure is characterized by covalent bonding between the metal ions (B and Ir) and the halogen ions (Cl). The creation of polar covalent bonds within the octahedral structure is attributed to the difference in electronegativity between the metal ions and Cl ions, as seen in prior studies.[54] The B–Ir bonding in the octahedral structure could also display metallic properties due to the overlap of their atomic orbitals. The distribution of charge density in materials is influenced by a combination of ionic, covalent, and metallic bonding interactions. The A ions generate a localized positive charge density, while the Cl ions create a localized negative charge due to their greater electronegativity. The unique bonding in A_2BIrCl_6 (A = Cs, Rb; B = Na, K), driven by covalent, ionic, and metallic interactions, is key to its excellent photovoltaic performance.

3.4 Optical properties

The exceptional optical properties of lead-free (non-toxic) double perovskites, such as A_2BIrCl_6 (A = Cs, Rb; B = Na, K), and their potential applications in photovoltaic and optoelectronic devices have attracted significant attention. To evaluate the optical behaviour of these compounds, the dielectric function, $\varepsilon(\omega)$, is computed. It is expressed as $\varepsilon(\omega) = \varepsilon_1(\omega) + i\varepsilon_2(\omega)$, where $\varepsilon_1(\omega)$ and $\varepsilon_2(\omega)$ represent the real and imaginary parts of the dielectric function, respectively.[55–57] The real part $\varepsilon_1(\omega)$ is calculated using the Kramers–Kronig relation:

$$\varepsilon_1(\omega) = 1 + \frac{2}{\pi} P \int_0^\infty \frac{\omega' \varepsilon_2(\omega')}{\omega'^2 - \omega^2} d\omega' \quad (7)$$

where P indicates the Cauchy principal value of the integral.

The imaginary part $\varepsilon_2(\omega)$ is determined from the momentum matrix elements of the occupied and unoccupied wave functions:[58,59]

$$\varepsilon_2(\omega) = \frac{2e^2\pi}{\Omega\varepsilon_0} \sum_{K,V,C} \left|\left\langle \psi_k^c | \hat{U} \cdot \vec{r} | \psi_k^V \right\rangle\right|^2 \delta\left(E_K^C - E_K^V - E\right) \quad (8)$$

In this equation, ω is the photon frequency, ψ_k^c and ψ_k^V are the wave functions of conduction and valence bands at wave vector k, e is the electronic charge, Ω is the unit cell volume, and $\hat{U}$ is the unit vector along the electric field polarization. The delta function δ ensures energy and momentum conservation during transitions between electronic states. The energies E_K^C and

E_K^V correspond to the conduction and valence band states at k, respectively.

The dielectric function is a crucial parameter that influences the charge-carrier recombination rate,[60] providing a clear understanding of the efficiency of optoelectronic devices.[61] Materials with higher static dielectric constants generally exhibit lower recombination rates, which enhances device performance. The real ($\varepsilon_1(\omega)$) and imaginary ($\varepsilon_2(\omega)$) components of the dielectric constant of A_2BIrCl_6 (A = Cs, Rb; B = Na, K) are depicted in Fig. 8a and b, respectively. The static dielectric function, $\varepsilon_1(0)$, for the investigated double perovskites is summarized as follows: $\varepsilon_1(0) = 2.78$ for $Cs_2NaIrCl_6$, $\varepsilon_1(0) = 2.77$ for Cs_2KIrCl_6, $\varepsilon_1(0) = 2.65$ for $Rb_2NaIrCl_6$, and $\varepsilon_1(0) = 2.68$ for Rb_2KIrCl_6. The relatively high $\varepsilon_1(0)$ values correspond to the materials' smaller band gaps, which are advantageous for reducing carrier recombination rates and enhancing optoelectronic device performance.[62] As photon energy increases, $\varepsilon_1(\omega)$ reaches its maximum value and then begins to decline, eventually attaining negative values. This signifies a transition from dielectric to metallic-like behavior. The crossover to negative $\varepsilon_1(\omega)$ values occurs at higher photon energies, indicating the energy threshold beyond which the materials lose their dielectric properties. This behavior demonstrates that A_2BIrCl_6 (A = Cs, Rb; B = Na, K) acts as a dielectric material up to the specified energy limits, making it suitable for optoelectronic applications within this energy range.

The imaginary part of the dielectric function, $\varepsilon_2(\omega)$, provides valuable insight into the electronic transitions between the valence and conduction bands. By examining $\varepsilon_2(\omega)$, one can relate these transitions to the band structure of A_2BIrCl_6 (A = Cs, Rb; B = Na, K). As depicted in Fig. 8(b), the values of $\varepsilon_2(\omega)$ remain negligible until reaching the band gap energy of each compound. At this point, significant peaks emerge, corresponding to the allowed transitions across the band gap. For $Cs_2NaIrCl_6$, Cs_2KIrCl_6, $Rb_2NaIrCl_6$, and Rb_2KIrCl_6, the notable peaks in $\varepsilon_2(\omega)$ arise as the photon energy surpasses the band gap, reflecting strong optical transitions. The peaks' locations correspond to prominent transitions involving Ir 5d and Cl 3p orbitals, which dominate the conduction and valence band states. The precise energy positions of these peaks highlight the interplay between the electronic structure and optical properties of the double perovskites, confirming the direct band gap nature of these compounds.

Fig. 8(c) displays the fluctuations of refractive index $n(\omega)$. The refractive index $n(\omega)$, which is directly related to $\varepsilon_1(0)$ as $n(0) = \sqrt{\varepsilon_1(0)}$,[63] is shown in Fig. 8(c). The behaviour of $\varepsilon_1(\omega)$ and $n(\omega)$ as functions of photon energy provides further insight into the dielectric properties of these materials. The static dielectric constants ($\varepsilon_1(0)$) and refractive indices ($n(0)$) indicate that $Cs_2NaIrCl_6$ and Cs_2KIrCl_6 exhibit slightly higher dielectric and refractive properties compared to their Rb-based counterparts, consistent with their lower band gaps. For A_2BIrCl_6 (A = Cs, Rb; B = Na, K), the $n(0)$ values range between 1.63 and 1.67, while the maximum $n(\omega)$ reaches approximately 2.4. These values indicate the dielectric behaviour of these materials and suggest their suitability for photovoltaic applications. The
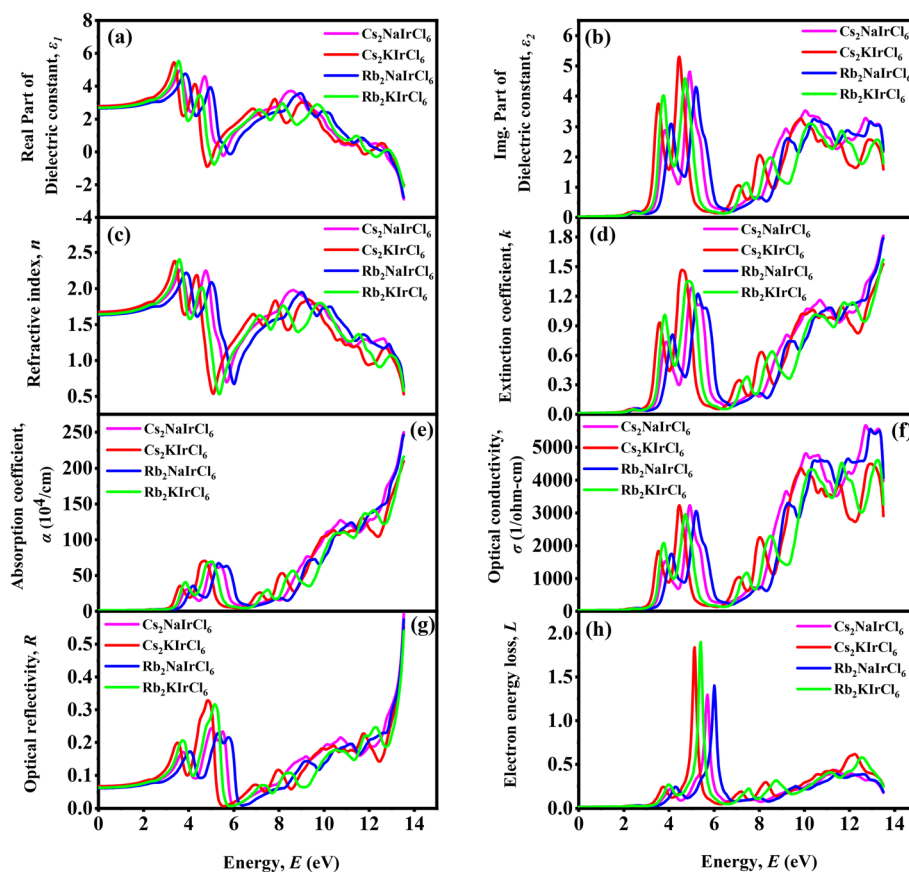
Fig. 8 (a) $\varepsilon_1(\omega)$: the real part of the dielectric constant, (b) $\varepsilon_2(\omega)$: imaginary part of the dielectric constant, (c) $n(\omega)$: refractive index and (d) $k(\omega)$: extinction coefficient, (e) $I(\omega)$: absorption coefficient, (f) $\sigma(\omega)$: real optical conductivity, (g) $R(\omega)$: optical reflectivity, and (h) $L(\omega)$: loss function for studied compounds.

moderate $n(0)$ values (between 1 and 2) and the maximum $n(\omega)$ values observed further confirm their potential for efficient light energy dispersion and absorption, essential characteristics for optoelectronic and energy-harvesting devices. The extinction coefficient, $k(\omega)$, quantifies the attenuation of electromagnetic radiation as it passes through a material. As shown in Fig. 8(d), the computed $k(\omega)$ values for A_2BIrCl_6 (A = Cs, Rb; B = Na, K) follow a trend similar to the imaginary part of the dielectric function, $\varepsilon_2(\omega)$. This correlation highlights the direct relationship between optical absorption and $k(\omega)$, as $\varepsilon_2(\omega)$ represents the material's ability to absorb energy from incident photons.

The Fig. 8(e) presents the absorption coefficient (α) as a function of photon energy (E) for A_2BIrCl_6 (A = Cs, Rb; B = Na, K) compounds. The absorption coefficient is a measure of how strongly a material absorbs light at a given energy. The absence of an electronic transition across the valence band to the conduction band was seen at incoming energy levels below the bandgap energy.

The optical conductivity $\sigma(\omega)$ for A_2BIrCl_6 (A = Cs, Rb; B = Na, K) is depicted in Fig. 8(f). As seen, the optical conductivity does not initiate at zero photon energy, a characteristic typical of semiconducting materials. Instead, the conductivity begins at specific photon energy thresholds, reflecting the materials' electronic band structures. For the compounds $Cs_2NaIrCl_6$,

Cs_2KIrCl_6, $Rb_2NaIrCl_6$, and Rb_2KIrCl_6, the optical conductivity demonstrates distinct trends across the photon energy range. The conductivity increases with photon energy, exhibiting peaks that align well with the electronic transitions predicted by band structure calculations. These peaks correspond to photon-induced excitations from the valence band to the conduction band.

The reflectivity (R) spectra for A_2BIrCl_6 (A = Cs, Rb; B = Na, K) are shown in Fig. 8(g), highlighting the optical response of these semiconducting compounds. At zero photon energy, the calculated static reflectivity values $R(0)$ is consistent across all compounds, as summarized in Table 4. Specifically, the values for $R(0)$ are 6% for all compounds.

Table 4 The calculated values of real part of dielectric constant $\varepsilon_1(0)$, refractive index $n(0)$, reflectivity $R(0)$ of A_2BIrCl_6 (A = Cs, Rb; B = Na, K) compounds

DP	$\varepsilon_1(0)$	$n(0)$	$R(0)$
$Cs_2NaIrCl_6$	2.78	1.67	0.06
Cs_2KIrCl_6	2.77	1.66	0.06
$Rb_2NaIrCl_6$	2.65	1.63	0.06
Rb_2KIrCl_6	2.68	1.64	0.06

The Fig. 8(f) depicts the loss function, $L(\omega)$, as a function of photon energy for A_2BIrCl_6 (A = Cs, Rb; B = Na, K). The loss function represents the energy loss of a fast electron traversing the material, and its peaks correspond to the plasmon resonance frequencies, which are indicative of collective oscillations of the electron density. The most notable peaks for all compounds are observed between 4.5 eV and 6 eV. These peaks signify the plasmon resonance frequencies and correspond to the materials' characteristic energy loss due to plasmon excitation. Among the compounds, $Rb_2NaIrCl_6$ exhibits a slightly higher loss peak compared to the others. At photon energies below 4 eV, $L(\omega)$ remains low, suggesting minimal energy loss due to electronic interactions in this range. This property makes these materials promising candidates for photovoltaic applications, where efficient light harvesting is crucial.[64] After the prominent peaks, $L(\omega)$ gradually decreases with increasing photon energy, indicating reduced plasmonic activity at higher photon energies. The compounds with higher $\varepsilon_1(0)$ (static dielectric constant) and lower band gaps tend to exhibit stronger and sharper plasmon peaks. This relationship correlates with the higher electron density contributing to the plasmon resonance.

3.5 Mechanical properties

Elastic constants are vital for understanding the mechanical behavior, stiffness, and stability of materials. For cubic systems like A_2BIrCl_6 (A = Cs, Rb; B = Na, K), only three independent elastic constants, C_{11}, C_{12}, and C_{44}, are relevant. These constants are crucial in evaluating material properties like brittleness, malleability, and anisotropy. Using finite strain theory,[65] the mechanical properties of A_2BIrCl_6 (A = Cs, Rb; B = Na, K) have been analyzed, providing insights into the compound's stability and response under applied forces, essential for potential engineering applications.

The mechanical stability of $Cs_2NaIrCl_6$, Cs_2KIrCl_6, $Rb_2NaIrCl_6$, and Rb_2KIrCl_6 is confirmed by meeting the Born stability criteria[66] as shown in Table 5. The calculated elastic constants indicate mechanical robustness, with $Cs_2NaIrCl_6$ and $Rb_2NaIrCl_6$ showing higher values of $C_{11} - C_{12}$, indicating greater stiffness. Similarly, the high $C_{11} + 2C_{12}$ values for these

compounds suggest strong resistance to deformation. The lower C_{44} for Rb_2KIrCl_6 indicates relatively reduced shear resistance compared to the others. The Cauchy pressure ($C_P = C_{12} - C_{44}$) is a key indicator of material brittleness and ductility. A positive C_P suggests ductility, while a negative C_P indicates brittleness. The calculated C_P values for A_2BIrCl_6 (A = Cs, Rb; B = Na, K) compounds are all negative are enlisted in Table 5. These results confirm their brittle nature, with Cs_2KIrCl_6 being the most brittle.

The mechanical properties of A_2BIrCl_6 (A = Cs, Rb; B = Na, K) are evaluated using estimated elastic constants, summarized in Table 5. The bulk modulus (B) measures the material's resistance to compression and is calculated using the formula:[67]

$$B = \frac{C_{11} + 2C_{12}}{3} \quad (9)$$

The shear modulus (G), Young's modulus (E), Poisson's ratio (ν), and other properties are computed using the Voigt–Reuss approach. The Voigt and Reuss methods for determining the moduli are given by:[68,69]

$$B_V = \frac{1}{3}(C_{11} + 2C_{12}) \quad (10)$$

$$G_V = \frac{1}{5}(C_{11} - C_{12} + 3C_{44}) \quad (11)$$

$$B_R = B_V = \frac{1}{3}(C_{11} + 2C_{12}) \quad (12)$$

$$G_R = \frac{5C_{44}(C_{11} - C_{12})}{[4C_{44} + 3(C_{11} - C_{12})]} \quad (13)$$

The final values of B and G are obtained by averaging the Voigt and Reuss results:

$$B = \frac{1}{2}(B_V + B_R) \quad (14)$$

$$G = \frac{1}{2}(G_V + G_R) \quad (15)$$

Table 5 The evaluated elastic constants C_{ij} (GPa) with Born stability criteria, Cauchy pressure, bulk modulus B (GPa), Shear modulus G (GPa), Young modulus Y (GPa), Poisson's ratio ν, Pugh's ratio B/G, and anisotropy coefficient A_Z of A_2BIrCl_6 (A = Cs, Rb; B = Na, K) compounds

Parameters		$Cs_2NaIrCl_6$	Cs_2KIrCl_6	$Rb_2NaIrCl_6$	Rb_2KIrCl_6
Born stability	C_{11} (GPa)	86.02	75.72	89.73	79.74
	C_{12} (GPa)	15.40	9.49	13.58	8.17
	C_{44} (GPa)	19.44	14.97	17.17	9.64
	$C_{11} - C_{12}$ (GPa)	70.62	66.23	76.15	71.57
	$C_{11} + 2C_{12}$ (GPa)	116.82	94.70	116.89	96.08
Cauchy pressure, C_P (GPa)		−4.04	−5.48	−3.59	−1.47
Bulk modulus, B (GPa)		38.94	31.57	38.96	32.03
Shear modulus, G (GPa)		24.74	20.70	23.77	20.10
Young modulus, Y (GPa)		61.26	50.96	59.26	43.04
Poisson's ratio, ν		0.24	0.23	0.25	0.24
Pugh's ratio, B/G		1.57	1.53	1.64	1.59
Zener anisotropy index, A_Z		0.55	0.45	0.45	0.27

Subsequently, Young's modulus (E) and Poisson's ratio (ν) are determined by the expressions:[70,71]

$$E = \frac{9BG}{3B + G} \quad (16)$$

$$\nu = \frac{(3B - 2G)}{2(3B + G)} \quad (17)$$

The estimated bulk moduli of A_2BIrCl_6 (A = Cs, Rb; B = Na, K) compounds, shown in Table 5, indicate that these materials are soft. Comparing the bulk modulus (B) with the shear modulus (G) reveals that for all compounds, $B > G$, suggesting that the mechanical strength is more influenced by shearing strain than volume strain. The bulk modulus is closely related to a material's atomic bond strength, as it inversely correlates with the unit cell volume and is linked to the cohesive or binding energy.[72,73] From Table 5, it is evident that Cs_2KIrCl_6 exhibits the highest atomic bonding strength, surpassing the other compounds in terms of its bulk modulus value (31.57 GPa), implying stronger atomic interactions in this compound compared to the others. The stiffness of a material is described by its Young's modulus (E), where a higher value indicates greater stiffness. In Table 5, $Cs_2NaIrCl_6$ has the highest Young's modulus (61.26 GPa), making it the stiffest among the compounds, while Rb_2KIrCl_6 has the lowest E value (43.04 GPa), indicating it is more flexible. The Young's modulus is critical for analyzing thermal shock resistance (R), as the critical R value is inversely proportional to E.[74] Thus, materials with a low E value, such as Rb_2KIrCl_6, exhibit higher thermal shock resistance compared to those with a higher E value like $Cs_2NaIrCl_6$.

Pugh's ratio (B/G) and Poisson's ratio (ν) are important indicators of a material's ductility or brittleness. For the compounds in Table 5, the Poisson's ratio values range from 0.23 to 0.25, while the Pugh's ratio ranges from 1.53 to 1.64. According to Pugh's criterion, a material is considered ductile if both $\nu > 0.26$ and $B/G > 1.75$.[67,75] Based on these criteria, all the titled compounds are classified as brittle.

The Zener anisotropy index (A_Z) is a key parameter used to understand the isotropy and anisotropy of a material. It is calculated using the equation:[75]

$$A_Z = \frac{2C_{44}}{C_{11} - C_{12}} \quad (18)$$

where a value of 1 indicates isotropic behaviour, and deviations from this value indicate varying degrees of anisotropy.[76,77] From Table 5, $Cs_2NaIrCl_6$ has a Zener anisotropy index of 0.55, indicating moderate anisotropyss. Cs_2KIrCl_6 and $Rb_2NaIrCl_6$, with A_Z values of 0.45, show similar, moderate anisotropic behavior. Rb_2KIrCl_6 has the lowest A_Z value of 0.27, suggesting it has the most pronounced anisotropy among the compounds, meaning its mechanical properties exhibit more directional dependence.

3.6 Thermodynamic properties

The thermodynamic properties of A_2BIrCl_6 (A = Cs, Rb; B = Na, K) perovskites, including density (ρ), sound velocities (v_l, v_t, v_m), Debye temperature (θ_D), melting temperature (T_m), minimum

Table 6 The computed density (ρ), longitudinal, transverse, and average sound velocities (v_l, v_t and v_m, respectively), Debye temperature (θ_D), minimum thermal conductivity (K_{min}), melting temperature (T_m), molar mass (M), Grüneisen parameter (γ) and lattice thermal conductivity (K_L) of A_2BIrCl_6 (A = Cs, Rb; B = Na, K) compounds

Parameters	$Cs_2NaIrCl_6$	Cs_2KIrCl_6	$Rb_2NaIrCl_6$	Rb_2KIrCl_6
$\rho \times 10^3$ (kg m^{-3})	4.41	4.12	3.95	3.67
v_l (m s^{-1})	4037.75	3794.49	4235.57	3851.50
v_t (m s^{-1})	2368.22	2244.38	2456.71	2142.20
v_m (m s^{-1})	2625.46	2486.22	2726.31	2385.66
θ_D (K)	263.48	241.82	276.67	234.49
$T_m \pm 300$ (K)	1061.35	1000.50	1083.31	1024.29
M (kg mole^{-1})	0.69	0.71	0.60	0.61
K_{min} (W m^{-1} K^{-1})	0.41	0.37	0.44	0.36
γ	1.45	1.41	1.50	1.65
K_L (W m^{-1} K^{-1})	1.64	1.43	1.51	0.78

thermal conductivity (k_{min}), and lattice thermal conductivity (K_L) are presented in Table 6. The methodology for these calculations is detailed in ref. 73 and 78. The Debye temperature, θ_D, represents the highest normal mode of vibration in a crystal and correlates with material hardness and thermal conductivity. For most crystals, the Debye temperature (θ_D) typically ranges between 200–400 K.[79] The estimated θ_D values for A_2BIrCl_6 (A = Cs, Rb; B = Na, K), as shown in Table 6, fall within this range. The values of θ_D range from 234.49 K (Rb_2KIrCl_6) to 276.67 K ($Rb_2NaIrCl_6$), indicating that all compounds are soft with low thermal conductivity. $Rb_2NaIrCl_6$ exhibits the highest θ_D, suggesting stronger bonding and greater hardness compared to others. Density (ρ) varies from 3.67 kg m^{-3} (Rb_2KIrCl_6) to 4.41 kg m^{-3} ($Cs_2NaIrCl_6$), while sound velocities (v_l, v_t, v_m) are consistent with the calculated Debye temperatures. These findings provide valuable insights into the thermal and mechanical behaviour of these compounds for further research.

The melting temperature (T_m) and minimum thermal conductivity (k_{min}) of A_2BIrCl_6 (A = Cs, Rb; B = Na, K) are shown in Table 6. The phonon mean free path has a strong influence on the lattice thermal conductivity. The lowest possible thermal conductivity may be attained if the phonon mean free path is like the interatomic distance. The calculated T_m values range from 1000.50 K (Cs_2KIrCl_6) to 1083.31 K ($Rb_2NaIrCl_6$), with $Rb_2NaIrCl_6$ having the highest melting point, suggesting stronger atomic interactions. The k_{min} values vary from 0.36 W m^{-1} K^{-1} (Rb_2KIrCl_6) to 0.44 W m^{-1} K^{-1} ($Rb_2NaIrCl_6$), indicating poor thermal conductivity across all compounds. The molar mass (M) ranges from 0.60 kg mole^{-1} ($Rb_2NaIrCl_6$) to 0.71 kg mole^{-1} (Cs_2KIrCl_6), aligning with the observed thermal properties. These findings highlight the compounds' low thermal conductivity and melting temperatures.

The lattice thermal conductivity (K_L) is crucial for evaluating thermoelectric properties and the efficiency of energy conversion in thermoelectric materials, especially under high-temperature applications. Low K_L is a prerequisite for materials intended for thermal insulation and thermoelectric devices.[80,81] Weak chemical bonding leads to strong lattice anharmonicity, which is closely linked to the Grüneisen parameter (γ) and affects thermal transport by enhancing

phonon scattering. At elevated temperatures, increased anharmonicity reduces phonon contribution to thermal conductivity. The parameters for A_2BIrCl_6 (A = Cs, Rb; B = Na, K) perovskites, shown in Table 6, indicate that K_L ranges from 0.78 W m^{-1} K^{-1} (Rb_2KIrCl_6) to 1.64 W m^{-1} K^{-1} ($Cs_2NaIrCl_6$). The Grüneisen parameter (γ) varies from 1.41 (Cs_2KIrCl_6) to 1.65 (Rb_2KIrCl_6), highlighting significant anharmonicity.

The thermodynamic potential of a system provides an in-depth view of its optimal behavior. By applying the quasi-harmonic method [82] and the computed phonon density of states, we calculate the thermodynamic potential for A_2BIrCl_6 (A = Cs, Rb; B = Na, K). The parameters considered include entropy (S), internal energy (E), Helmholtz free energy (F), and specific heat (C_v), which are calculated using the following equations. [83]

$$F = 3nNk_BT = \int_0^{\omega_{max}} \ln\left(2 \sinh \sinh\left(\frac{\hbar\omega}{2k_BT}\right)\right) g(\omega) d\omega \quad (19)$$

$$E = 3nN\frac{\hbar}{2} \int_0^{\omega_{max}} \omega \coth\left(\frac{\hbar\omega}{2k_BT}\right) g(\omega) d\omega, \quad (20)$$

$$S = 3nNk_B \int_0^{\omega_{max}} \left[\frac{\hbar\omega}{2k_BT}\coth\left(\frac{\hbar\omega}{2k_BT}\right)\right.$$
$$\left. - \ln\left(2\sinh\left(\frac{\hbar\omega}{2k_BT}\right)\right)\right] g(\omega) d\omega \quad (21)$$

$$C_v = 3nNk_B \int_0^{\omega_{max}} \left(\frac{\hbar\omega}{2k_BT}\right)^2 \left(\frac{\hbar\omega}{2k_BT}\right) g(\omega) d\omega, \quad (22)$$

In these equations, k_B refers to the Boltzmann constant, N stands for Avogadro's number, n indicates the number of atoms in each unit cell, w denotes the phonon frequency, w_{max} is the maximum phonon frequency, and $g(w)$ is the normalized density of states for phonons. With,

$$\int_0^{\omega_{max}} g(\omega) d\omega = 1 \quad (23)$$

Fig. 9 and 10 display the computed values of F, E, S, and C_v across a temperature range from 0 K to 1000 K. The Helmholtz free energy (F) of A_2BIrCl_6 (A = Cs, Rb; B = Na, K) is shown in Fig. 10, displaying a steady decrease with increasing temperature. The reduction in free energy is a natural phenomenon, where it becomes more negative as the process progresses. The data indicates that enthalpy, entropy, and heat capacity increase as temperature rises.

The thermodynamic behavior of solids can be understood by analyzing their specific heat, which indicates their heat retention ability. Our findings reveal that the heat capacity of the material increases more prominently compared to its enthalpy and entropy, indicating that the A_2BIrCl_6 (A = Cs, Rb; B = Na, K) systems are highly responsive to temperature changes. As the temperature rises, the heat capacity gradually increases, eventually stabilizing at approximately 58 ($Cs_2NaIrCl_6$), 57 (Cs_2KIrCl_6), 58 ($Rb_2NaIrCl_6$), and 57 (Rb_2KIrCl_6) cal per cell K. This value is frequently identified as the Dulong–Petit limit. [84] The Debye temperature (θ_D) serves as a vital parameter in numerous thermophysical properties. Higher (θ_D) values usually correlate
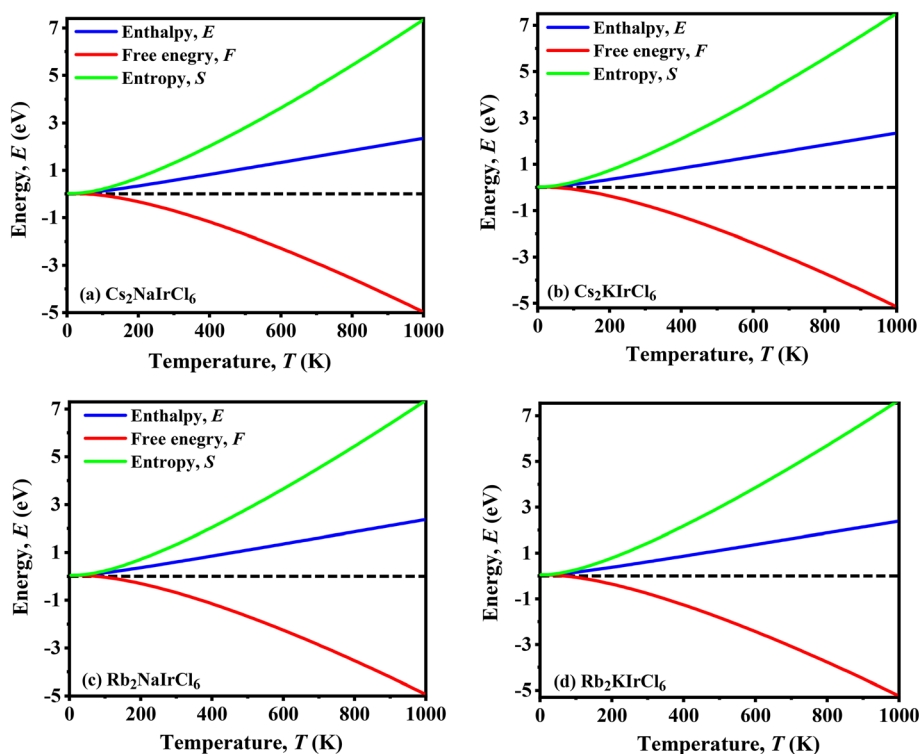

Fig. 9 The temperature-dependent variations of the computed thermodynamic parameters enthalpy (E), free energy (F), and entropy (S) for A_2BIrCl_6 (A = Cs, Rb; B = Na, K) at zero pressure.
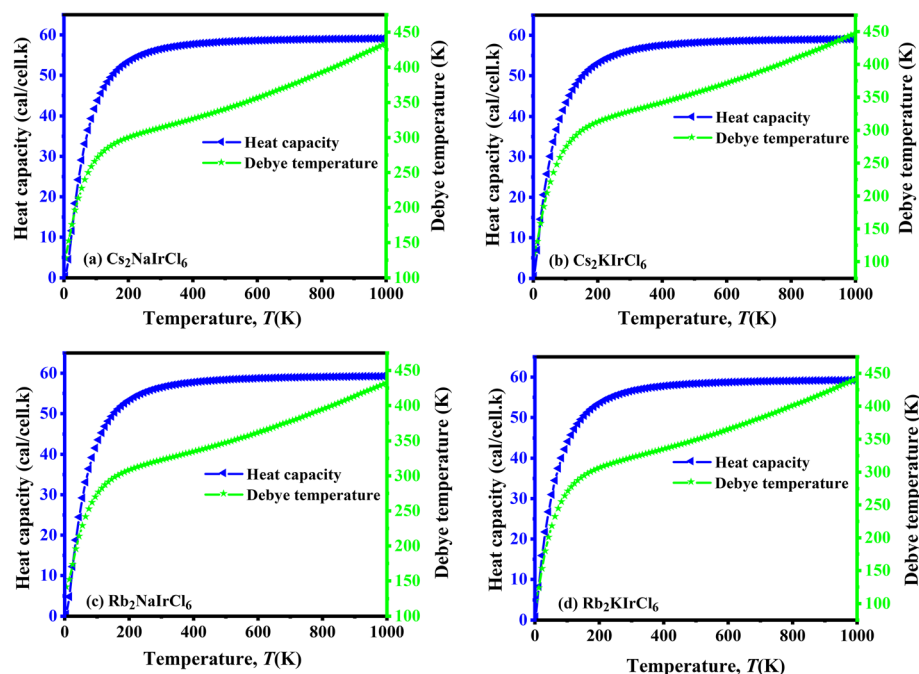
Fig. 10 The temperature-dependent variations of the computed thermodynamic parameters heat capacity and Debye temperature for A_2BIrCl_6 (A = Cs, Rb; B = Na, K) at zero pressure.

with more robust atomic bonding and a greater phonon role in heat conduction. For all the compounds examined, the Debye temperature grows with increasing temperature. The maximum Debye temperature for all studied compounds is around 450 K at 1000 K.

4. Conclusion

This study presents the first exploration of four novel double halide perovskites, A_2BIrCl_6 (A = Cs, Rb; B = Na, K), and investigates their structural, electronic, optical, mechanical, and thermo-physical properties, providing essential insights into their potential applications. The stability of the cubic phase structure is validated through several criteria, including tolerance factors between 0.88 and 0.98, as well as octahedral factors ranging from 0.47 to 0.57. The assessment of their thermodynamic stability and dynamic equilibrium was based on their positive phonon dispersion, along with negative formation and binding energies. These materials exhibit semiconducting properties, with a direct band gap identified at the X–X symmetry k-points. The energy band gaps calculated for $Cs_2NaIrCl_6$, Cs_2KIrCl_6, $Rb_2NaIrCl_6$, and Rb_2KIrCl_6 are 1.927 eV, 1.991 eV, 2.025 eV, and 2.102 eV, respectively, making them highly suitable for use in solar cell and optoelectronics applications. Additionally, the investigation of their optical properties highlighted significant visible light absorption (up to 10^4 cm^{-1}) and minimal reflectivity, pointing to their potential as highly effective absorber layers in solar cell applications. The elastic constants Poisson's ratio, Pugh's ratio, and Cauchy pressure obtained from the study suggest that the perovskites analyzed exhibit mechanical stability, though they demonstrate

brittle characteristics. The thermodynamic characteristics of A_2BIrCl_6 (A = Cs, Rb; B = Na, K), including specific heat, Helmholtz free energy, internal energy, entropy, Debye temperature, melting point, minimum thermal conductivity, lattice thermal conductivity, and the Grüneisen parameter, indicate their thermodynamic stability. These findings indicate that the titled double perovskite materials are potential candidates for optoelectronic and photovoltaic applications.

Data availability

The data supporting this study's findings are available from the corresponding author upon reasonable request.

Author contributions

Investigation was led by Md. Tarekuzzaman, who also contributed to methodology development, data curation, conceptualization, and drafting of the original manuscript. Nazmul Shahadath participated in formal analysis, methodology development, data curation, and manuscript review and editing. Formal analysis was conducted by Mufrat Montasir, who also provided software support, contributed to conceptualization, and participated in manuscript review and editing. O. Alsalmi provided validation and conducted formal analysis. M. H. Mia engaged in formal analysis, contributed to methodology development, data curation, and manuscript review and editing. Hmoud Al-Dmour provided validation and conducted formal analysis. Md. Rasheduzzaman conducted formal analysis, provided validation, and participated in manuscript review and editing. Md. Zahid Hasan conducted formal analysis, provided

validation, supervised the study, and participated in manuscript review and editing.

Conflicts of interest

There is no conflict to declare.

Acknowledgements

References

1 W.-J. Yin, B. Weng, J. Ge, Q. Sun, Z. Li and Y. Yan, Oxide Perovskites, Double Perovskites and Derivatives for Electrocatalysis, Photocatalysis, and Photovoltaics, *Energy Environ. Sci.*, 2019, **12**(2), 442–462.

2 C. Bogmans, *et al.*, *Energy, Efficiency Gains and Economic Development: When Will Global Energy Demand Saturate?*, 2020.

3 W.-J. Yin, J.-H. Yang, J. Kang, Y. Yan and S.-H. Wei, Halide Perovskite Materials for Solar Cells: A Theoretical Review, *J. Mater. Chem. A*, 2015, **3**(17), 8926–8942.

4 J. Song, J. Li, X. Li, L. Xu, Y. Dong and H. Zeng, Quantum Dot Light-Emitting Diodes Based on Inorganic Perovskite Cesium Lead Halides (CsPbX3), *Adv. Mater.*, 2015, **27**(44), 7162–7167.

5 S. A. Veldhuis, P. P. Boix, N. Yantara, M. Li, T. C. Sum, N. Mathews and S. G. Mhaisalkar, Perovskite Materials for Light-Emitting Diodes and Lasers, *Adv. Mater.*, 2016, **28**(32), 6804–6834.

6 S. M. H. Qaid, Q. ul Ain, H. M. Ghaithan, I. Mursaleen, A. Ahmed Ali Ahmed and J. Munir, First-Principles Investigations on the Structural, Optoelectronic, Mechanical and Transport Properties of New Stable Lead-Free Double Perovskites Cs2BB′I6 (B = Ag/Rb, B′ = Bi/Ga) Halides, *Mater. Sci. Eng. B*, 2024, **301**, 117176.

7 H. Murtaza, Q. ul Ain, J. Munir, H. M. Ghaithan, A. A. A. Ahmed and S. M. H. Qaid, Exploring the Optoelectronic Attributes, Thermoelectric and Photocatalytic Potential of Double Perovskites Cs2BB'H6 (B = Al, Na and B'=Tl, In): A DFT Study, *Mater. Sci. Eng. B*, 2024, **301**, 117171.

8 H. Murtaza, J. Munir, H. M. Ghaithan, Q. ul Ain, A. A. A. Ahmed and S. M. H. Qaid, Scrutinize the Physical Attributes of Thermodynamically and Elastically Stable Double Perovskite Oxides Ba2CdXO6 (X = Mo, U) for Optoelectronics, Photocatalytic and Green Technology, *Comput. Mater. Sci.*, 2024, **232**, 112674.

9 Q. Mahmood, G. M. Mustafa, M. Morsi, H. Albalawi, T. H. Flemban, M. Hassan, H. Althib, M. I. Khan and T. Ghrib, Theoretical Investigations of Optoelectronic and Thermoelectric Properties of Halide Based Double Perovskite Halides: K2TeX6, *Phys. Scr.*, 2021, **96**(7), 075703.

10 L. Mao, S. M. L. Teicher, C. C. Stoumpos, R. M. Kennard, R. A. DeCrescent, G. Wu, J. A. Schuller, M. L. Chabinyc, A. K. Cheetham and R. Seshadri, Chemical and Structural Diversity of Hybrid Layered Double Perovskite Halides, *J. Am. Chem. Soc.*, 2019, **141**(48), 19099–19109.

11 S. M. H. Qaid, M. Jamil, J. Munir, H. M. Ghaithan, A. A. A. Ahmed and Q. ul Ain, A Computational Insight into Rb2ASbX6 (A=Tl, Cu & X=I, Cl) Double Perovskites for Energy Storage and Optoelectronic Applications, *Phys. Scr.*, 2023, **98**(10), 105910.

12 M. T. Anderson, K. B. Greenwood, G. A. Taylor and K. R. Poeppelmeier, B-Cation Arrangements in Double Perovskites, *Prog. Solid State Chem.*, 1993, **22**(3), 197–233.

13 R. D. Nelson, K. Santra, Y. Wang, A. Hadi, J. W. Petrich and M. G. Panthani, Synthesis and Optical Properties of Ordered-Vacancy Perovskite Cesium Bismuth Halide Nanocrystals, *Chem. Commun.*, 2018, **54**(29), 3640–3643.

14 L. A. Muscarella and E. M. Hutter, Halide Double-Perovskite Semiconductors beyond Photovoltaics, *ACS Energy Lett.*, 2022, **7**(6), 2128–2135.

15 N. J. Jeon, J. H. Noh, W. S. Yang, Y. C. Kim, S. Ryu, J. Seo and S. I. Seok, Compositional Engineering of Perovskite Materials for High-Performance Solar Cells, *Nature*, 2015, **517**(7535), 476–480.

16 J. Munir, M. K. Iftikhar, M. I. Jamil, M. U. Din, T. Alshahrani, H. I. Elsaeedy and Q. Ain, Physical Properties of Elastically and Thermodynamically Stable Magnetic AcXO3 (X = Cr, Fe) Perovskite Oxides: A DFT Investigation, *Phys. Scr.*, 2023, **98**(6), 065513.

17 J. Munir, M. Mustafa, H. Naeem, M. Yousaf, E. F. El-Shamy and Q. Ain, Electronic Structure, Optical and Thermal Response of Lead-Free RbAuBr3 and RbAuBr4 Perovskites for Renewable Energy Applications, *ECS J. Solid State Sci. Technol.*, 2022, **11**(12), 123003.

18 S. A. Dar and B. Want, Direct Band Gap Double Perovskite Halide Cs2ScInCl6 for Optoelectronic Applications—A First Principle Study, *Comput. Condens. Matter.*, 2022, **33**, e00736.

19 H. Zhou, Q. Chen, G. Li, S. Luo, T. Song, H.-S. Duan, Z. Hong, J. You, Y. Liu and Y. Yang, Interface Engineering of Highly Efficient Perovskite Solar Cells, *Science*, 2014, **345**(6196), 542–546.

20 M. Saliba, T. Matsui, K. Domanski, J.-Y. Seo, A. Ummadisingu, S. M. Zakeeruddin, J.-P. Correa-Baena, W. R. Tress, A. Abate, A. Hagfeldt and M. Grätzel, Incorporation of Rubidium Cations into Perovskite Solar Cells Improves Photovoltaic Performance, *Science*, 2016, **354**(6309), 206–209.

21 A. Al-Ashouri, E. Köhnen, B. Li, A. Magomedov, H. Hempel, P. Caprioglio, J. A. Márquez, A. B. Morales Vilches, E. Kasparavicius, J. A. Smith, N. Phung, D. Menzel, M. Grischek, L. Kegelmann, D. Skroblin, C. Gollwitzer, T. Malinauskas, M. Jošt, G. Matič, B. Rech, R. Schlatmann, M. Topič, L. Korte, A. Abate, B. Stannowski, D. Neher, M. Stolterfoht, T. Unold, V. Getautis and S. Albrecht, Monolithic Perovskite/Silicon Tandem Solar Cell with

>29% Efficiency by Enhanced Hole Extraction, *Science*, 2020, **370**(6522), 1300–1309.

22 S. De Wolf, J. Holovsky, S.-J. Moon, P. Löper, B. Niesen, M. Ledinsky, F.-J. Haug, J.-H. Yum and C. Ballif, Organometallic Halide Perovskites: Sharp Optical Absorption Edge and Its Relation to Photovoltaic Performance, *J. Phys. Chem. Lett.*, 2014, **5**(6), 1035–1039.

23 C. C. Stoumpos, C. D. Malliakas and M. G. Kanatzidis, Semiconducting Tin and Lead Iodide Perovskites with Organic Cations: Phase Transitions, High Mobilities, and Near-Infrared Photoluminescent Properties, *Inorg. Chem.*, 2013, **52**(15), 9019–9038.

24 O. A. Lozhkina, A. A. Murashkina, M. S. Elizarov, V. V. Shilovskikh, A. A. Zolotarev, Yu. V. Kapitonov, R. Kevorkyants, A. V. Emeline and T. Miyasaka, Microstructural Analysis and Optical Properties of the Halide Double Perovskite Cs2BiAgBr6 Single Crystals, *Chem. Phys. Lett.*, 2018, **694**, 18–22.

25 X.-G. Zhao, J.-H. Yang, Y. Fu, D. Yang, Q. Xu, L. Yu, S.-H. Wei and L. Zhang, Design of Lead-Free Inorganic Halide Perovskites for Solar Cells via Cation-Transmutation, *J. Am. Chem. Soc.*, 2017, **139**(7), 2630–2638.

26 E. T. McClure, M. R. Ball, W. Windl and P. M. Woodward, Cs2AgBiX6 (X = Br, Cl): New Visible Light Absorbing, Lead-Free Halide Perovskite Semiconductors, *Chem. Mater.*, 2016, **28**(5), 1348–1354.

27 A. J. Kale, R. Chaurasiya and A. Dixit, Inorganic Lead-Free Cs2AuBiCl6 Perovskite Absorber and Cu2O Hole Transport Material Based Single-Junction Solar Cells with 22.18% Power Conversion Efficiency, *Adv. Theory Simul.*, 2021, **4**(3), 2000224.

28 R. E. Brandt, R. C. Kurchin, R. L. Z. Hoye, J. R. Poindexter, M. W. B. Wilson, S. Sulekar, F. Lenahan, P. X. T. Yen, V. Stevanović, J. C. Nino, M. G. Bawendi and T. Buonassisi, Investigation of Bismuth Triiodide (BiI3) for Photovoltaic Applications, *J. Phys. Chem. Lett.*, 2015, **6**(21), 4297–4302.

29 G. Volonakis, A. A. Haghighirad, R. L. Milot, W. H. Sio, M. R. Filip, B. Wenger, M. B. Johnston, L. M. Herz, H. J. Snaith and F. Giustino, Cs2InAgCl6: A New Lead-Free Halide Double Perovskite with Direct Band Gap, *J. Phys. Chem. Lett.*, 2017, **8**(4), 772–778.

30 B. Nath, B. Pradhan and S. K. Panda, Optical Tunability of Lead Free Double Perovskite Cs2AgInCl6via Composition Variation, *New J. Chem.*, 2020, **44**(43), 18656–18661.

31 B. Yang and K. Han, Charge-Carrier Dynamics of Lead-Free Halide Perovskite Nanocrystals, *Acc. Chem. Res.*, 2019, **52**(11), 3188–3198.

32 J. C. Dahl, W. T. Osowiecki, Y. Cai, J. K. Swabeck, Y. Bekenstein, M. Asta, E. M. Chan and A. P. Alivisatos, Probing the Stability and Band Gaps of Cs2AgInCl6 and Cs2AgSbCl6 Lead-Free Double Perovskite Nanocrystals, *Chem. Mater.*, 2019, **31**(9), 3134–3143.

33 M. G. B. Ashiq, Q. Mahmood, T. Zelai, O. Hakami, N. A. Kattan, H. Albalawi, A. I. Aljameel, S. Bouzgarrou, T. Ghrib and K. I. Hussein, The Narrow Band Bap Double Perovskites X2CuInCl6 (X = K, Rb, Cs) for Optoelectronics,

34 D. Behera, B. Mohammed, S. Taieb, B. Mokhtar, S. Al-Qaisi and S. K. Mukherjee, First-Principle Investigations on Optoelectronics and Thermoelectric Properties of Lead-Free Rb2InSbX6 (X = Cl, Br) Double Perovskites: For Renewable Energy Applications, *Eur. Phys. J. Plus*, 2023, **138**(6), 520.

35 A. Ayyaz, G. Murtaza, M. Shafiq, M. Qasim Shah, N. Sfina and S. Ali, Exploring Structural, Thermodynamic, Elastic, Electro-Optic, and Thermoelectric Characteristics of Double Perovskites Rb2XInBr6 (X = Na, K) for Photovoltaic Applications: A DFT Approach, *Sol. Energy*, 2023, **265**, 112131.

36 M. Zia ur Rehman, S. A. M. Abdelmohsen, E. A. Mahmoud, M. U. Saeed, M. Idress, M. Shafiq, B. Amin and Y. Saeed, First Principles Study of Structural, Electronic, Elastic and Optical Properties of Cs2LiTlBr6 and Cs2NaTlBr6, *Mater. Sci. Semicond. Process.*, 2022, **151**, 106993.

37 S. H. Shah, P. song, T. Huang, S. Shakeel, S. Khan, M. W. Ashraf and G. Murtaza, Comprehensive Study of Structural, Elastic, Electronic, Optical, and Thermoelectric Properties of Rb2NaTlZ6 (Z = Cl, Br, and I) by DFT, *Mater. Sci. Semicond. Process.*, 2024, **178**, 108400.

38 H. Murtaza, Q. Ain, J. Munir, H. M. Ghaithan, M. Ali, A. A. Ali Ahmed, H. Qaid and S. M. H. Qaid, Tuning the Thermoelectric and Optoelectronic Attributes of Lead-Free Novel Fluoroperovskites Cs2BB'F6 (B = Rb, In, Na and B'=Ir, As, Rh): A First-Principles Investigation, *J. Phys. Chem. Solids*, 2024, **190**, 111934.

39 P. Hohenberg and W. Kohn, Inhomogeneous Electron Gas, *Phys. Rev.*, 1964, **136**(3B), B864–B871.

40 W. Kohn and L. J. Sham, Self-Consistent Equations Including Exchange and Correlation Effects, *Phys. Rev.*, 1965, **140**(4A), A1133–A1138.

41 K. Schwarz, DFT Calculations of Solids with LAPW and WIEN2k, *J. Solid State Chem.*, 2003, **176**(2), 319–328.

42 J. P. Perdew, K. Burke and M. Ernzerhof, Generalized Gradient Approximation Made Simple, *Phys. Rev. Lett.*, 1996, **77**(18), 3865–3868.

43 F. D. Murnaghan, The Compressibility of Media under Extreme Pressures, *Proc. Natl. Acad. Sci. U. S. A.*, 1944, **30**(9), 244–247.

44 F. Tran and P. Blaha, Accurate Band Gaps of Semiconductors and Insulators with a Semilocal Exchange-Correlation Potential, *Phys. Rev. Lett.*, 2009, **102**(22), 226401.

45 K. Momma and F. Izumi, VESTA 3 for Three-Dimensional Visualization of Crystal, Volumetric and Morphology Data, *J. Appl. Crystallogr.*, 2011, **44**(6), 1272–1276.

46 M. D. Segall, P. J. D. Lindan, M. J. Probert, C. J. Pickard, P. J. Hasnip, S. J. Clark and M. C. Payne, First-Principles Simulation: Ideas, Illustrations and the CASTEP Code, *J. Phys.:Condens. Matter*, 2002, **14**(11), 2717.

47 I. Borriello, G. Cantele and D. Ninno, Ab Initio Investigation of Hybrid Organic-Inorganic Perovskites Based on Tin Halides, *Phys. Rev. B:Condens. Matter Mater. Phys.*, 2008, **77**(23), 235214.

48 X. Du, D. He, H. Mei, Y. Zhong and N. Cheng, Insights on Electronic Structures, Elastic Features and Optical Properties of Mixed-Valence Double Perovskites Cs2Au2X6 (X=F, Cl, Br, I), *Phys. Lett. A*, 2020, **384**(8), 126169.

49 V. M. Goldschmidt, Die Gesetze der Krystallochemie, *Naturwissenschaften*, 1926, **14**(21), 477–485.

50 C. J. Bartel, C. Sutton, B. R. Goldsmith, R. Ouyang, C. B. Musgrave, L. M. Ghiringhelli and M. Scheffler, New Tolerance Factor to Predict the Stability of Perovskite Oxides and Halides, *Sci. Adv.*, 2019, **5**(2), eaav0693.

51 C. Li, X. Lu, W. Ding, L. Feng, Y. Gao and Z. Guo, Formability of ABX3 (X = F, Cl, Br, I) Halide Perovskites, *Acta Crystallogr., Sect. B*, 2008, **64**(6), 702–707.

52 A. Togo and I. Tanaka, First Principles Phonon Calculations in Materials Science, *Scr. Mater.*, 2015, **108**, 1–5.

53 C. Kittel and P. McEuen, *Introduction to Solid State Physics*, John Wiley & Sons, 2018.

54 M. Wuttig, *et al.*, Halide perovskites: Advanced photovoltaic materials empowered by a unique bonding mechanism, *Adv. Funct. Mater.*, 2022, **32**(2), 2110166.

55 A. A. Mubarak, The First-Principle Study of the Electronic, Optical and Thermoelectric Properties of XTiO3 (X = Ca, Sr and Ba) Compounds, *Int. J. Mod. Phys. B*, 2016, **30**(20), 1650141.

56 K. E. Babu, *et al.*, First-principles study of electronic structure and optical properties of cubic perovskite CsCaF3, *Chin. Phys. Lett.*, 2012, **29**(11), 117102.

57 M. A. Green, Y. Jiang, A. M. Soufiani and A. Ho-Baillie, Optical Properties of Photovoltaic Organic–Inorganic Lead Halide Perovskites, *J. Phys. Chem. Lett.*, 2015, **6**(23), 4774–4785.

58 C. Ambrosch-Draxl and J. O. Sofo, Linear Optical Properties of Solids within the Full-Potential Linearized Augmented Planewave Method, *Comput. Phys. Commun.*, 2006, **175**(1), 1–14.

59 N. V. Smith, Photoelectron Energy Spectra and the Band Structures of the Noble Metals, *Phys. Rev. B*, 1971, **3**(6), 1862–1878.

60 X. Liu, B. Xie, C. Duan, Z. Wang, B. Fan, K. Zhang, B. Lin, F. J. M. Colberts, W. Ma, R. A. J. Janssen, F. Huang and Y. Cao, A High Dielectric Constant Non-Fullerene Acceptor for Efficient Bulk-Heterojunction Organic Solar Cells, *J. Mater. Chem. A*, 2018, **6**(2), 395–403.

61 S. Saha, T. P. Sinha and A. Mookerjee, Electronic Structure, Chemical Bonding, and Optical Properties of Paraelectric ${\mathrm{BaTiO}}_{3}$, *Phys. Rev. B:Condens. Matter Mater. Phys.*, 2000, **62**(13), 8828–8834.

62 S. Zuhair Abbas Shah, S. Niaz, T. Nasir and S. M. Ramay, Exploring the Structural, Phononic, Electronic, Magnetic, Optical, and Thermoelectric Properties of Pb-Free Vanadium-Based Double Perovskites Using the First-Principles Approach for Optoelectronic and Thermoelectric Applications, *Sol. Energy*, 2022, **240**, 27–37.

63 G. Murtaza, A. A. AlObaid, T. I. Al-Muhimeed, S. Al-Qaisi, A. Rehman, H. H. Hegazy, G. Nazir, M. Morsi and Q. Mahmood, Tailoring of Band Gap to Tune the Optical and Thermoelectric Properties of Sr1-xBaxSnO3 Stannates

for Clean Energy; Probed by DFT, *Chem. Phys.*, 2021, **551**, 111322.

64 S. Z. A. Shah, A. Afzal, F. Khan, S. Zafar, J. Sifuna, A. A. Nassani, S. U. Asif and Z. Abbas, Small Band Gap Pb-Free Double Perovskites X2NaSbBr6 (X=Na, Li): A Study of the Stabilities, Opto-Electronic and Thermoelectric Aspects from the First-Principles Approach, *Comput. Condens. Matter.*, 2025, **42**, e01001.

65 F. D. Murnaghan, Finite Deformations of an Elastic Solid, *Am. J. Math.*, 1937, **59**(2), 235–260.

66 M. Born, On the Stability of Crystal Lattices. I, *Math. Proc. Camb. Philos. Soc.*, 1940, **36**(2), 160–172.

67 I. N. Frantsevich, *Elastic Constants and Elastic Moduli of Metals and Insulators*, 1982.

68 A. Reuss, Berechnung Der Fließgrenze von Mischkristallen Auf Grund Der Plastizitätsbedingung Für Einkristalle, *J. Appl. Math. Mech.*, 1929, **9**(1), 49–58.

69 R. Hill, The Elastic Behaviour of a Crystalline Aggregate, *Proc. Phys. Soc. Sect. A*, 1952, **65**(5), 349.

70 M. Al-Fahdi, A. Rodriguez, T. Ouyang and M. Hu, High-Throughput Computation of New Carbon Allotropes with Diverse Hybridization and Ultrahigh Hardness, *Crystals*, 2021, **11**(7), 783.

71 G. Vaitheeswaran, V. Kanchana, A. Svane and A. Delin, Elastic Properties of MgCNi3—a Superconducting Perovskite, *J. Phys.:Condens. Matter*, 2007, **19**(32), 326214.

72 D. G. Clerc and H. M. Ledbetter, Mechanical Hardness: A Semiempirical Theory Based on Screened Electrostatics and Elastic Shear, *J. Phys. Chem. Solids*, 1998, **59**(6), 1071–1095.

73 M. A. Khatun, M. H. Mia, M. A. Hossain, F. Parvin and A. K. M. A. Islam, Optical and Thermoelectric Properties of Layer Structured Ba2XS4 (X = Zr, Hf) for Energy Harvesting Applications, *J. Phys. Chem. Solids*, 2025, **196**, 112381.

74 X. Wang, H. Xiang, X. Sun, J. Liu, F. Hou and Y. Zhou, Mechanical Properties and Damage Tolerance of Bulk Yb3Al5O12 Ceramic, *J. Mater. Sci. Technol.*, 2015, **31**(4), 369–374.

75 S. F. Pugh, XCII. Relations between the Elastic Moduli and the Plastic Properties of Polycrystalline Pure Metals, *Lond. Edinb. Dublin Philos. Mag. J. Sci.*, 1954, **45**(367), 823–843.

76 H. Ledbetter and A. Migliori, A General Elastic-Anisotropy Measure, *J. Appl. Phys.*, 2006, **100**(6), 063516.

77 S. I. Ranganathan and M. Ostoja-Starzewski, Universal Elastic Anisotropy Index, *Phys. Rev. Lett.*, 2008, **101**(5), 055504.

78 M. H. K. Rubel, M. A. Hossain, M. K. Hossain, K. M. Hossain, A. A. Khatun, M. M. Rahaman, Md. Ferdous Rahman, M. M. Hossain and J. Hossain, First-Principles Calculations to Investigate Structural, Elastic, Electronic, Thermodynamic, and Thermoelectric Properties of CaPd3B4O12 (B = Ti, V) Perovskites, *Results Phys.*, 2022, **42**, 105977.

79 O. L. Anderson, A Simplified Method for Calculating the Debye Temperature from Elastic Constants, *J. Phys. Chem. Solids*, 1963, **24**(7), 909–917.

80 W. Lee, H. Li, A. B. Wong, D. Zhang, M. Lai, Y. Yu, Q. Kong, E. Lin, J. J. Urban, J. C. Grossman and P. Yang, Ultralow Thermal Conductivity in All-Inorganic Halide Perovskites, *Proc. Natl. Acad. Sci. U. S. A.*, 2017, **114**(33), 8693–8697.

81 Q. Yan and M. G. Kanatzidis, High-Performance Thermoelectrics and Challenges for Practical Devices, *Nat. Mater.*, 2022, **21**(5), 503–513.

82 C. Lee and X. Gonze, Ab Initio Calculation of the Thermodynamic Properties and Atomic Temperature Factors of ${\mathrm{SiO}}_{2}$ \ensuremath{\alpha}-Quartz and Stishovite, *Phys. Rev. B:Condens. Matter Mater. Phys.*, 1995, **51**(13), 8610–8613.

83 S. Baroni, S. de Gironcoli, A. Dal Corso and P. Giannozzi, Phonons and Related Crystal Properties from Density-Functional Perturbation Theory, *Rev. Mod. Phys.*, 2001, **73**(2), 515–562.

84 D. Wu, S. Huang, D. Feng, B. Li, Y. Chen, J. Zhang and J. He, Revisiting AgCrSe2 as a Promising Thermoelectric Material, *Phys. Chem. Chem. Phys.*, 2016, **18**(34), 23872–23878.